Resolving double-peaked emission line galaxies using MaNGA

I. Star formation, quenching and the connection to galaxy physical properties

Barbara Mazzilli Ciraulo[1], Anne-Laure Melchior[1], Françoise Combes[1,2], and Daniel Maschmann[1]

[1] LERMA, Sorbonne Université, Observatoire de Paris, Université PSL, CNRS, F-75014, Paris, France
e-mail: `Barbara.Mazzilli-Ciraulo@observatoiredeparis.psl.eu`
[2] Collège de France, 11 Place Marcelin Berthelot, 75005 Paris, France

ABSTRACT

Star formation quenching in spiral galaxies could be due to supernovae or active galaxy nuclei (AGN) feedback, but also due to the environment. To probe the influence of minor mergers, we have selected a sample of massive galaxies in the Sloan Digital Sky Survey presenting double-peaked emission lines in their centre. Within these nearby galaxies, the star formation regulation is studied together with their physical properties: morphology, environment, colour, stellar age and star formation rate versus AGN diagnostics. We want to study both the global galactic properties as well as the resolved maps tracing the gas ionisation. We therefore gather a sample of 29 star-forming galaxies from the Mapping Nearby Galaxies at APO (MaNGA) survey that exhibit central double-peaked emission lines. We define control samples of single-peaked emission line galaxies which match the same stellar mass and redshift distribution. We find that the double-peaked emission-line galaxies exhibit a higher fraction of galaxies in the green valley defined by the NUV-r colour than the control sample. This green colour is due to a contribution from old stellar populations hosted in these overall star-forming galaxies. Relying on the resolved power of MaNGA integral field spectroscopic data, we show that this sample host two types of galaxies: some have a nuclear AGN-like activity and some are inactive. This AGN excitation is correlated to the $D_n(4000)$ index tracing the age of the stellar population. We discuss that we are sampling different phases of evolution of these galaxies known to be isolated or in poor groups. Minor mergers are known to provide gas in the central regions of the merger remnant, coming in part from the companion, but also mainly from the gas reservoir of the primary galaxy's outskirts. This merging activity is acting in two phases: in the first one, the gas driven inwards triggers star formation in the centre, while the disc is replenished from the outer gas reservoir. The galaxies appear in the blue-cloud category. Then, the central gas ignites (weakly) a nuclear AGN-activity, quenching inside-out the star formation, and the galaxy enters the green valley category. In the second phase, the gas remaining in the disc converges towards the nucleus, reignites star formation, while the disc is now depleted, lacking the gas reservoir to be replenished. These green-valley galaxies appear then quenched outside-in. This scenario is compatible with other studies discussing central activities due to minor mergers.

Key words. Galaxies: star formation quenching – Methods: data analysis – Techniques: integral field spectroscopy

1. Introduction

The observation of large galaxy samples showed that galaxies in the Local Universe follow a bi-modal distribution in the colour-magnitude and colour-mass diagrams (Blanton et al. 2011; Baldry et al. 2004). The two main populations correspond to a "blue cloud" with galaxies characterised by active star formation, and a "red sequence", referring to passive galaxies; while the region lying between these two groups is called "green valley" (Salim 2014). This latter region may be defined in the UV-optical colour-magnitude diagram and is considered as a way to pinpoint transitional galaxies (Salim 2014), lying below the star-forming sequence but yet not completely passive. The bi-modality is found to depend on evolutionary stage but also on morphology (discs dominating in the blue cloud and spheroids in the red sequence), even though no specific Hubble type has been observed among the green-valley galaxies. These objects thought to be in transition are thus critical to the understanding of the paths from the active sequence to quiescence.

The termination of star formation activity, or quenching, plays a key role in this transition. However, this process remains an open question, as the mechanisms involved are numerous and complex. For instance, the environment can reduce the gas fraction in galaxy clusters, through ram-pressure stripping (Boselli et al. 2016) or strangulation (Weinmann et al. 2009). Hence, high-density environments reduce star formation and shorten the quenching timescale (e.g. Coenda et al. 2018). Other mechanisms can stop the star formation activity, such as morphological quenching (Martig et al. 2009) which corresponds to the stabilisation of the gas due to bulge growth and/or bar-driven processes, which prevents the gas from collapsing and forming stars. Saintonge et al. (2011) also showed that the molecular gas depletion time is longer at high stellar masses. They, furthermore, discuss a possible AGN contribution as one of the processes responsible for the quenching. On the one hand, Barrows et al. (2017) found a positive correlation between the specific star formation rate and AGN luminosity but on the other hand, Kaviraj et al. (2015) showed that nearby merger-triggered AGN are unlikely to provide strong regulation in the star formation process, given the different timescales involved. Gas depletion appears to be one of the most obvious mechanism leading to star formation quenching but the removal of the gas itself can be

caused by different phenomena as ram-pressure stripping, viscous stripping or strangulation. The former is the most efficient in rich galaxy clusters but Rasmussen et al. (2008) showed that it is not sufficient to explain gas depletion in compact groups. The two latter are then proposed to interpret the gas depletion.

Tidal interactions and merging processes can drive the gas towards the centre of galaxies, which triggers a starburst and thus enhances central star formation on a relatively short time-scale (Di Matteo et al. 2008; Patton et al. 2011). This subsequent active star formation will finally consume the gas reservoir and result in the final quenching. Identifying and studying galaxy pairs or at least interacting galaxies thus appear crucial to investigate the star formation cycle of galaxies. For spectacular systems such as the Antennae (Whitmore et al. 2014; Lahén et al. 2018), the Taffy galaxies (Condon et al. 1993) or IIZw096 (Inami et al. 2010), the merging process is obvious. In parallel, for other objects with no morphological signatures, it can be challenging to unveil an ongoing merger event, especially a minor merger. Investigating the gas kinematics is necessary. Some complex emission line profiles can be used as a tracers of galaxy interactions, such as the double-peaked (DP) emission lines. A systematic search for these features was performed in Ge et al. (2012) and more detailed works on the origin of double-peaked profiles were mostly focused on dual AGN (e.g. Comerford et al. 2012; Nevin et al. 2018).

Based on the asset that double-peaked emission lines can trace key processes of galaxy evolution, Maschmann et al. (2020) selected 5663 galaxies from the Reference Catalogue of Spectral Energy Distribution (RCSED, Chilingarian et al. 2017) exhibiting such line shapes. They developed an automated selection procedure to find DP galaxies without relying on a visual inspection of the spectra. These DP galaxies display significant differences compared to a control sample which was selected following the same stellar mass and redshift distributions: they mostly evolve in isolated environment, but show a significant excess of S0 galaxies, a large stellar velocity dispersion and an enhanced central star formation activity. No dependency on inclination is found, discarding a simple scenario of a rotating disc. The authors, thus, argue that this sample corresponds to a minor-merger sequence as suggested in Bournaud et al. (2007) (see details in Maschmann et al. 2020). More detailed studies on smaller galaxy samples, such as Comerford et al. (2018) were able to identify a past merger as the underlying process of the observed DP emission lines. Similarly, Maschmann & Melchior (2019) found different excitations in the two emission line components of DP galaxies manifesting the two progenitors of a galaxy merger. A more detailed analysis with spatially-resolved spectroscopic observations succeeded in decomposing two kinematic components (Mazzilli Ciraulo et al. 2021). They associated the two components to two galaxies in the act of merging, creating DP emission line features. However, it is still challenging to conclude on the underlying process leading to DP emission lines in large galaxy samples since many effects such as a rotating inner disc or nuclear outflows can be responsible for DP emission lines (detailed discussion in Maschmann et al. 2020, hereafter M20).

The emergence and availability of large integral field spectroscopic surveys enable the nature of the closest galaxies (at $z < 0.14$) exhibiting these DP emission line profiles to be investigated in further details. We, therefore, cross-identified the galaxies of the DP catalogue mentioned above with the targets encompassed in the summary file from the MaNGA Data Reduction Pipeline (DRP, Law et al. 2016) of the SDSS Data Release 15 (Aguado et al. 2019). We identified a sample of 29 nearby galax-

ies located at an average redshift of 0.0653 (D_L=254.7 Mpc) (hereafter called the DP/MaNGA sample). This paper is the first of a series of three papers dedicated to the study of this sample. As described below, the present paper is focused on the analysis of the star formation properties of this galaxy sample, with a focus on the green valley definition. The second one is based on the analysis of CO and HI observations of this sample, and will discuss the Schmidt-Kennicutt relation and the star formation efficiency. The last one is focused on the kinematic signatures and particularities of these galaxies.
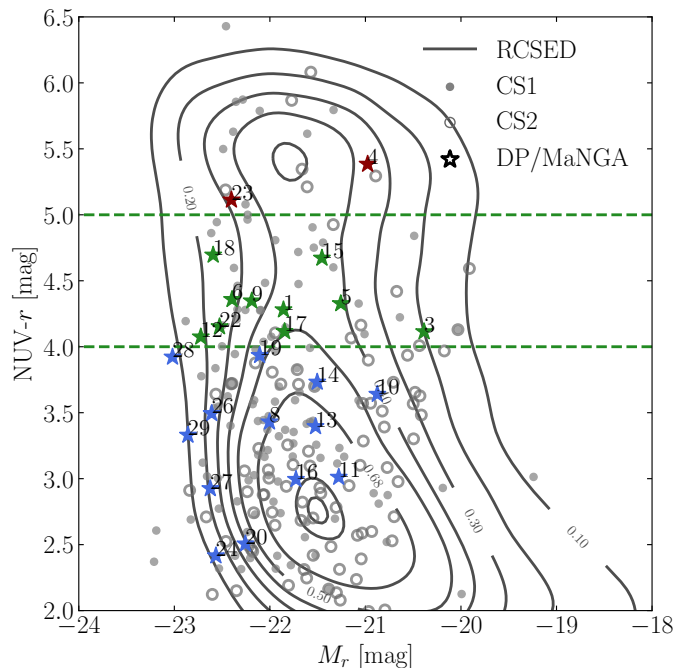

Fig. 1: Colour-magnitude diagram. The colour NUV-r is taken from the RCSED catalogue (Chilingarian et al. 2017) and is K- and dust-corrected. The M_r magnitude is the r absolute magnitude.

In Sect. 2, we describe the DP/MaNGA sample and the data gathered for the corresponding galaxies. We also define control samples of single-Gaussian-shaped emission-line galaxies that will be used for comparison. In Sect. 3, we explore the properties of these 29 DP/MaNGA galaxies in contrast to the control samples. We quantify the impact of AGN activity on the star formation and test different quenching mechanisms in Sect. 4. In Sect. 5, we discuss how these galaxies fit in the more general evolution of star formation quenching in galaxies, followed by a conclusion in Sect. 6.

A cosmology of $\Omega_m = 0.3$, $\Omega_\Lambda = 0.7$ and $H_0 = 0.7$ is assumed throughout this work.

2. Sample and data description

2.1. DP/MaNGA sample

Mapping Nearby Galaxies at APO (MaNGA, Bundy et al. 2015) is part of the fourth generation of SDSS (SDSS-IV, Blanton et al. 2017) and consists of an integral field unit survey targeting local (0.01 < z < 0.15) galaxies with stellar masses $M_\star \geq 10^9 M_\odot$. The observations are performed using integral field units (IFUs) of different sizes, from 19 to 127 fibres corresponding to an outer-on-sky diameter from 12.5 to 32.5″ (Drory et al. 2015). The

Table 1: The DP/MaNGA sample

ID	designation	z	$M_\star$ $\log_{10}(M_\odot)$	SFR $M_\odot$ yr^{-1}	i $^\circ$	env.	morph.	colour-sSFR
(1)	(2)	(3)	(4)	(5)	(6)	(7)	(8)	(9)
G1	J110649.16+455752.6	0.02490	10.99	1.21	32	cluster, cent.	E	GV, TZ
G2	J110704.17+454919.6	0.02521	10.85	2.07	80	cluster, sat.	LTG	*GV*
G3	J101954.80+361932.7	0.02612	10.10	2.33	76	isolated	S0	GV
G4	J074953.38+451454.6	0.03126	10.61	0.01	40	isolated	S0	red sequence
G5	J133213.69+265659.9	0.03529	10.47	2.18	65	poor group, cent.	LTG	GV
G6	J121810.50+442401.7	0.03826	11.30	1.18	46	poor group, cent.	S0	GV, TZ
G7	J080136.97+185306.6	0.03915	10.93$^{(!)}$	0.80$^{(!)}$	52	isolated	M	*GV, TZ*
G8	J161652.01+501655.9	0.04168	11.09	1.89	64	cluster, sat.	LTG	blue cloud, TZ
G9	J143031.19+524225.8	0.04488	11.09	0.63	51	cluster, sat.	LTG	GV, TZ
G10	J112525.63+515302.0	0.04912	10.53	2.06	77	isolated	LTG	active
G11	J075114.77+280913.0	0.05232	10.74	1.43	58	isolated	LTG	active
G12	J125448.95+440920.2	0.05432	11.36	1.50	71	isolated	LTG	GV, TZ
G13	J161552.50+440940.8	0.05484	10.93	3.69	67	isolated	LTG	blue cloud
G14	J072717.73+434705.5	0.05645	10.96	2.66	66	isolated	S0	active
G15	J161224.61+483147.6	0.05779	10.85	0.90	66	poor group, sat.	LTG	GV, TZ
G16	J041006.33-060305.9	0.05781	10.72	7.96	49	isolated	E	blue cloud
G17	J154308.66+400254.8	0.06256	10.97	6.22	54	isolated	S0	GV
G18	J015122.27+130337.3	0.06416	11.26	11.51	66	poor group, cent.	LTG	GV
G19	J120611.03+450857.1	0.06654	10.89	8.30	50	poor group, cent.	E	blue cloud
G20	J101211.76+450831.8	0.07643	11.09	10.38	46	poor group, cent.	LTG	blue cloud
G21	J080010.14+191403.6	0.07821	11.32$^{(!)}$	11.43$^{(!)}$	55	poor group, cent.	M	*GV*
G22	J160739.28+232500.8	0.08746	11.26	3.15	65	cluster, sat.	LTG	GV
G23	J161956.57+244440.2	0.08812	11.26	1.63	34	rich group, cent.	E	red sequence, TZ
G24	J221024.49+114247.0	0.09228	11.20	13.27	–	isolated	M$^{(\star)}$	AS
G25	J153521.83+270728.8	0.09373	10.91$^{(!)}$	17.96$^{(!)}$	63	poor group, cent.	LTG	*blue cloud*
G26	J154637.06+434101.2	0.10117	11.30	8.71	55	poor group, cent.	LTG	blue cloud
G27	J083635.38+230710.5	0.12522	11.33	16.75	43	isolated$^{(Y)}$	M	blue cloud
G28	J145252.45+451405.3	0.13265	11.39	10.69	38	isolated$^{(Y)}$	LTG	blue cloud
G29	J213002.45+002751.1	0.13506	11.32	9.06	35	isolated$^{(Y)}$	LTG	blue cloud

Notes: (1) Arbitrary identifier, (2) SDSS name, (3) SDSS redshift, (4) stellar mass computed by Salim et al. (2016), except for the G7, G21 and G25 with a $^{(!)}$ whose stellar mass comes from Kauffmann et al. (2003a), (5) star formation rate from Salim et al. (2016), except for galaxies marked with a $^{(!)}$ for which SFR is from Brinchmann et al. (2004), (6) inclination angle computed using the measurements from Fischer et al. (2019), (7) galaxy environment as found in Saulder et al. (2016) except for the three last objects, with $^{(Y)}$, whose environment comes from Yang et al. (2007), (8) morphology classification based on the probabilities provided in the MaNGA Deep Learning DR15 Morphology catalogue, relying on the measurements from Fischer et al. (2019), except for G24 that we classify manually and that is marked with $^{(\star)}$, (9) classification based on the NUV-r vs. specific Star Formation Rate (sSFR) diagram: blue cloud, green valley (GV), red sequence, transition zone (TZ).

spectra are observed in the range of 3600 to 10400 Å with an averaged spectral resolution of R~2000 and a mean spatial resolution of 2.5″. Individual fibre spectra are re-arranged into a data cube with 0.5″ × 0.5″ spaxels. The MaNGA data are well-suited to study the ionised gas, namely its distribution, kinematics and excitation within the observed sources. Value-added catalogues are available for MaNGA galaxies and make possible to investigate the photometry measurements, morphology (MaNGA Py-Morph DR15 photometric catalogue, Fischer et al. 2019), as well as stellar properties and global properties (MaNGA Pipe3D, Sánchez et al. 2016a,b) of the targets.

In order to study DP galaxies in greater detail, we cross match the DP catalogue of Maschmann et al. (2020) with the MaNGA DR15 catalogue and find 29 DP galaxies observed by MaNGA. These galaxies are listed in Table 1 and are sorted by redshift.

In Fig. 1 we show the colour-magnitude diagram for the DP/MaNGA and the control samples (see Sect. 2.2). We use dust- and K-corrected r-band and NUV magnitudes provided by the RCSED catalogue (Chilingarian et al. 2017). We compute

the absolute magnitude from the apparent magnitude following Eq. (1) of Wyder et al. (2007). The contours correspond to 10^5 galaxies representative of the RCSED catalogue (Chilingarian et al. 2017). The coloured stars (resp. grey dots and solid circles) are the DP/MaNGA (resp. CS1 and CS2) galaxies discussed in Sect. 2.2. Following Salim (2014), we categorise galaxies into the red sequence characterised by colours NUV-$r > 5$, the so called green valley (GV) with $4 < NUV − r < 5$ and the blue cloud at NUV − $r < 4$. Beside two galaxies (G4 and G23), the majority is situated in the blue cloud and a significant fraction is found in the GV. In the following, we will adopt the colour code defined in this figure: blue for the blue cloud, green for GV galaxies and dark red for the red sequence.

2.2. Selection of the control samples

To find the particularities of the DP/MaNGA galaxies, we define two control samples of galaxies exhibiting a single-peaked emission line inside the central 3″ spectrum. Following the procedure described in Maschmann et al. (2020), we select the galaxies for
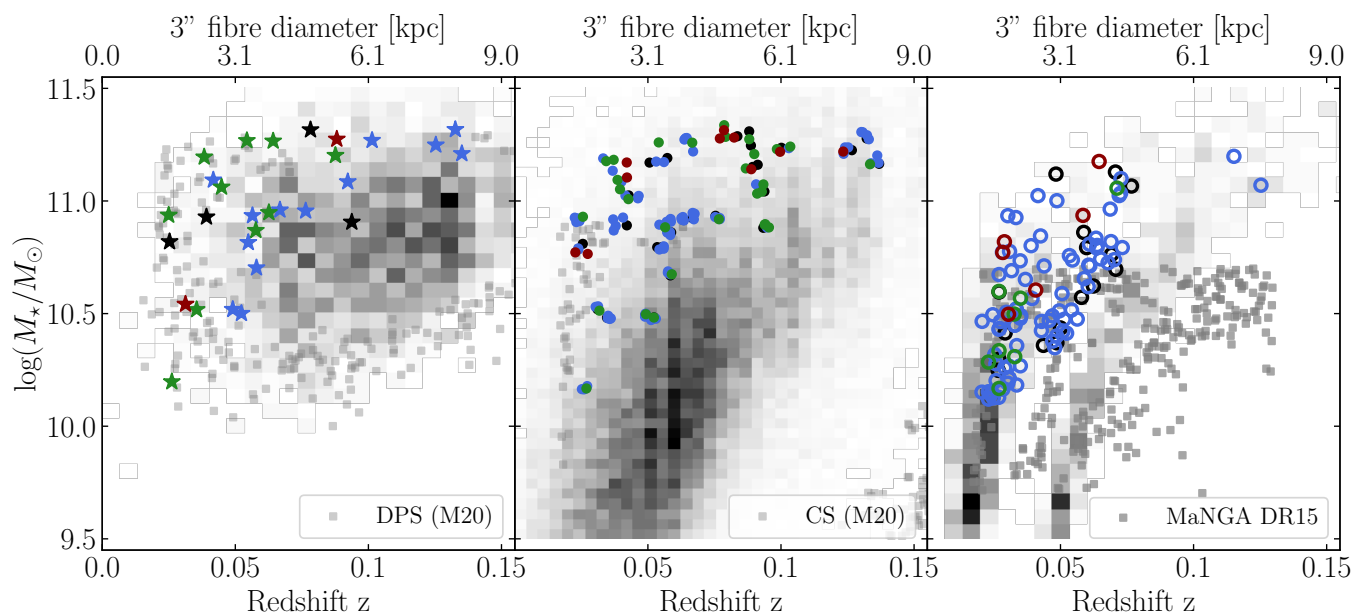
Fig. 2: Distribution in the $M_\star - z$ plane of the DP/MaNGA (colour-coded stars on left panel), CS1 (colour-coded filled circles on middle panel) and CS2 (colour-coded empty circles on right panel) galaxies. These three samples are respectively superimposed on the DPS distribution, the CS from Maschmann et al. (2020), and the whole MaNGA sample (Bundy et al. 2015). The colour-coding refers to the NUV-r colour: ★blue-cloud galaxies, ★green-valley galaxies; ★ red-sequence galaxies; ★ no NUV-r measurement available.)
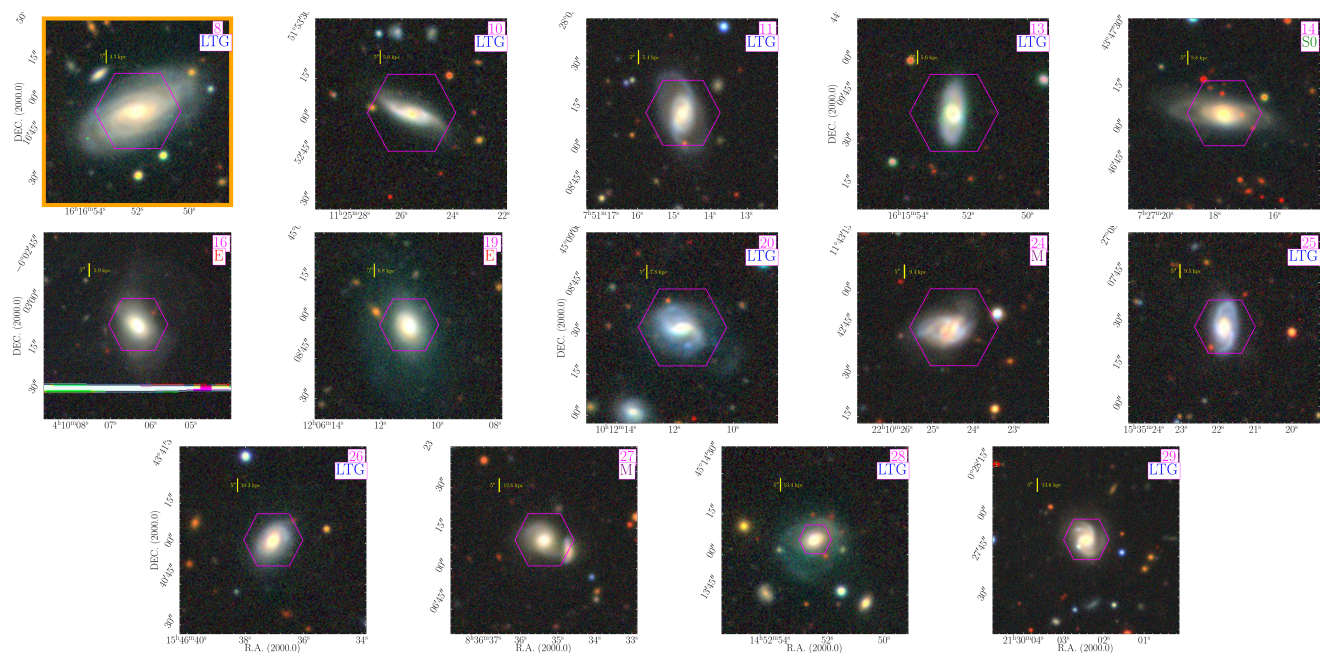
Fig. 3: 62x62″ Legacy survey snapshots of the galaxies belonging to the blue sequence, based on NUV-r colour, among the DP/MaNGA galaxies. The corresponding MaNGA IFU footprint in magenta and the morphological type are shown for each source. The galaxy displayed with an orange frame is the one in the transition zone in terms of sSFR ($-11.8 < \log(\text{sSFR}) < -10.8$). The galaxies are sorted by redshift, from left to right, top to bottom.

our control samples following the same redshift and stellar mass $M_\star$ distribution as the DP/MaNGA sample. We start from the control sample (CS) defined by Maschmann et al. (2020) which consists of 89 412 galaxies characterised by a single-Gaussian shaped emission line in the 3″ SDSS fibre. Since the CS is dominated by galaxies with smaller stellar masses in comparison to

the DP/MaNGA sample we are limited in the number of galaxies with the same redshift and stellar mass distribution.

We select a first control sample (hereafter CS1), consisting of 143 galaxies from the CS of M20, i.e. galaxies with single-Gaussian-shaped emission lines in their single SDSS spectrum. As shown in Fig. 2, the CS1 shows only small deviations in redshift and stellar mass in comparison to the DP/MaNGA. To en-
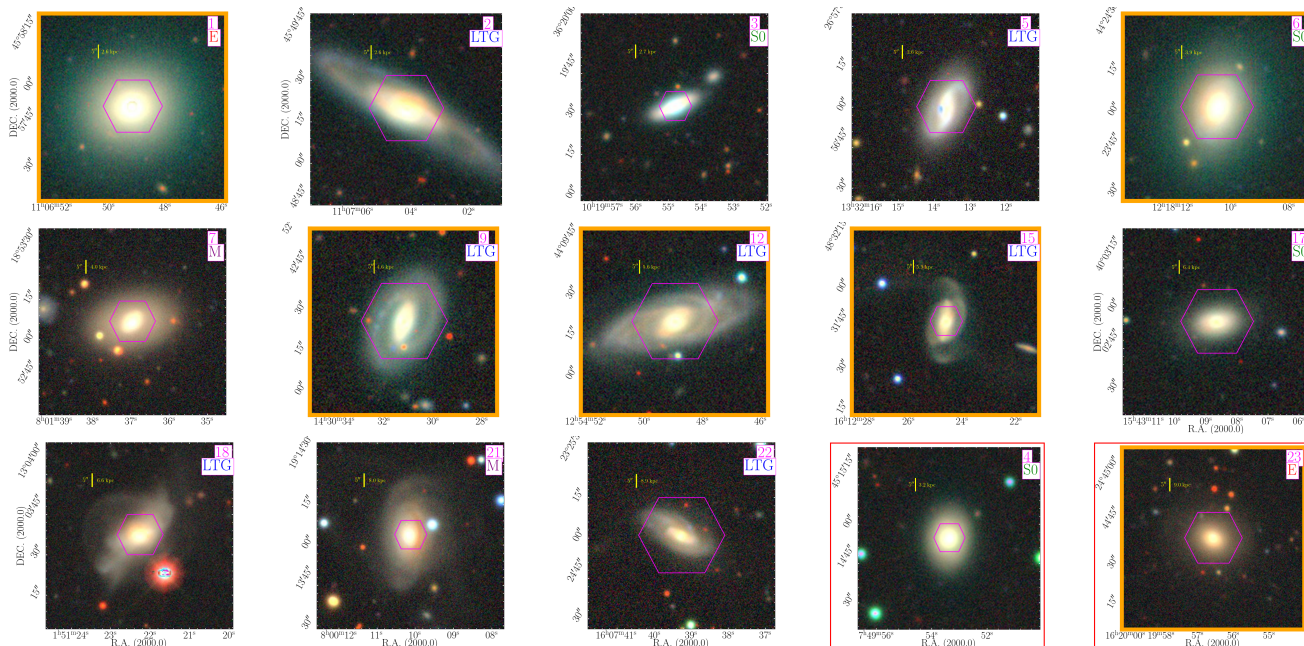
Fig. 4: Same as Fig. 3 but for the green-valley galaxies and the red galaxies (with the red frames). The panels surrounded with an orange frame are the green-valley galaxies not in the transition region.

able a comparison with MaNGA observations between galaxies exhibiting a central single- or a double-peaked emission line, we select a second control sample (hereafter CS2). Therefore, we cross-match the CS with the MaNGA DR15 catalogue and select again galaxies following the same redshift and stellar mass distribution as the DP/MaNGA sample. We finally select the CS2 consisting of 109 galaxies. As shown in Fig. 2, the CS2 comprises less massive galaxies than the CS1. This is due to the fact that at higher masses only a few galaxies with a single-peaked central emission line profile was observed by MaNGA. In order to visualise the samples selected for this work in contrast to the samples of Maschmann et al. (2020) and the MaNGA DR15 we show their stellar mass-redshift distribution in Fig. 2.

2.3. Other archival data

To discuss the physical properties of the DP/MaNGA galaxies, we make use of different catalogues.

Salim et al. (2016) analysed GALEX, SDSS and WISE data and built a catalogue from them, that encompasses stellar mass, dust attenuation, star formation rate for $\sim 7 \cdot 10^5$ galaxies. They used a Chabrier initial mass function (IMF) (Chabrier 2003). Three galaxies out of the DP/MaNGA are not included in their data set (G7, G21 and G25). For those latter three galaxies, we rely on the star formation rate estimates computed by Brinchmann et al. (2004), and available through the MPA-JHU DR7 release of spectrum measurements[1]. These latter SFR estimates are derived using a Kroupa initial mass function (Kroupa 2001), and this data set also comprises stellar mass estimates based on fits to the photometry following Kauffmann et al. (2003a). As precised in Salim et al. (2016), a -0.025 dex offset is applied when comparing these different SFR estimates, to adjust from the Kroupa to Chabrier IMF. We adopt the Salim et al. (2016) estimate as far as possible, since it is using $22\mu m$ photometry and hence minimises possible dust extinction/emission biases.

We also use the $D_n(4000)$ index from MPA-JHU DR7 catalogue, to discuss the stellar ages of the galaxies.

The Reference Catalogue of Spectral Energy Distributions (RCSED, Chilingarian et al. 2017) encompasses 800 299 galaxies at low and intermediate redshift and provides for each spectrophotometric measurements from different surveys as well as value-added data such as K-correction, emission line flux measurements, gas-phase metallicity, extinction.

2.4. MaNGA data products

We aim at deriving spatially-resolved as well as global properties of the DP/MaNGA galaxies. We use the final data cubes provided by the Data Reduction Pipeline (DRP, Law et al. 2016) that are logarithmic sampled and the maps provided by the Data Analysis Pipeline (DAP, Westfall et al. 2019). Briefly, each spectrum of the 3D data is fitted using the penalized PiXel-Fitting routine (pPXF, Cappellari & Emsellem 2004; Cappellari 2017): the stellar continuum is adjusted by fitting 49 families of stellar spectra from the MILES library (Falcón-Barroso et al. 2011) and then subtracted to the observed spectrum. The nebular emission lines in the resulting spectrum are fitted using a Gaussian function. The MaNGA DAP proposes two analysis methods to derive physical quantities: the Voronoi-binned maps for which a Voronoi binning scheme has been applied and has associated the summed flux to each spaxel belonging to the same spatial bin; the hybrid maps for which a similar Voronoi binning scheme has been applied for stellar properties but for which emission line measurements are proceeded spaxel-by-spaxel. We also exploit the stellar continuum measurements and the derived stellar mass density provided in the value-added catalogue Pipe3D for MaNGA DR15 (Sánchez et al. 2016b, 2018). We aim at computing quantities like specific star-formation rate for which we make use of the stellar mass measurements of Pipe3D, whose procedure does not proceed to the same binning scheme. Therefore, we decide to work with the hybrid-scheme maps and spaxel-by-spaxel emission line measurements.
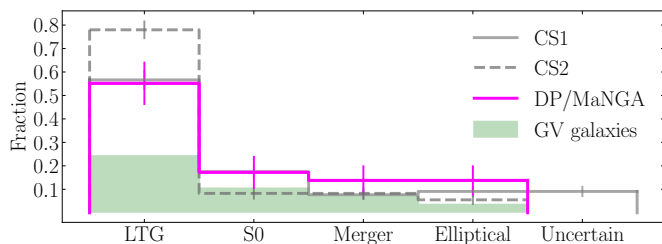
---

[1] https://wwwmpa.mpa-garching.mpg.de/SDSS/DR7/

Fig. 5: Morphology distribution for the 29 DP/MaNGA galaxies (in pink), 143 CS1 galaxies (in solid grey) and 109 CS2 galaxies (in dashed grey). The filled histogram corresponds to the green valley DP/MaNGA galaxies. The error bars represent the binomial errors.

3. DP/MaNGA sample properties

3.1. Morphology

A visual inspection of the RGB images provided by the Legacy survey (Dey et al. 2019) reveals that our sample gathers a diversity of galaxy types, namely late-type galaxies (LTG), elliptical galaxies and disrupted galaxies which are most likely mergers. We display the Legacy survey snapshots in Fig. 3 and 4 and mark for each galaxy the corresponding MaNGA IFU footprint with a magenta hexagon. The two figures are sorted according to their NUV-*r* colour, as displayed in Fig. 1. We present the morphological classification of the DP/MaNGA sample in Table 1 and mark the morphological type of each galaxy in the top right of their snapshot in Figs. 3 and 4.

3.1.1. Methodology

Fischer et al. (2019) performed a Sérsic (as well as a Sérsic + an exponential) fit of the 2D surface brightness profiles for all MaNGA DR15 galaxies. They used the python package PY-MORPH[2] and added improvements compared to the fitting procedure presented in Meert et al. (2015). We use the calculated semi-minor over semi-major axis ratio (b/a) to compute the inclination angle i following:

$$\cos(i) = \sqrt{\frac{(b/a)^2 - q_0^2}{1 - q_0^2}} \qquad (1)$$

where q_0 is the intrinsic axial ratio of edge-on galaxies, set to $q_0 = 0.2$ (Holmberg 1958).

We make use of the companion catalogue, MaNGA Deep Learning DR15 Morphology catalogue, which encompasses machine learning based morphological classifications (Domínguez Sánchez et al. 2018). This catalogue covers MaNGA galaxies that were not processed in former bulge-disc decomposition catalogues based on SDSS DR7 photometry. We use the following galaxy type probabilities computed by (Domínguez Sánchez et al. 2018): the T-Type to estimate the morphological type on the Hubble Sequence, P_{S0} denoting the probability to detect a S0 galaxy and P_{merg} giving the probability to detect a galaxy merger. We follow the recommended criteria to classify the galaxies of our sample as:

- Late-Type Galaxies (LTGs): T-Type > 0 ;
- Early-Type Galaxies (ETGs): T-Type ≤ 0 ;
  - S0: T-Type ≤ 0 and P_S0 > 0.5 ;

---

[2] https://pypi.org/project/pymorph/

- Ellipticals (E): T-Type ≤ 0 and P_S0 ≤ 0.5.

We also set our own criterion to define an object as a merger:

- Merger: P_merg > 0.9.

Fischer et al. (2019) precise that the given probability of merger signature indicates projected close pairs or nearby objects rather than ongoing merger events and find that 11% of the whole MaNGA sample have P_merg > 0.8. To be restrictive, we select the criterion P_merg > 0.9 to classify a source as a merger. In our sample, the three galaxies with the highest merger probabilities evolve in an isolated environment or in a poor group according to Saulder et al. (2016) and Yang et al. (2007), but the Legacy survey snapshots show projected close-by objects for galaxy 27 of the DP/MaNGA sample. Moreover, the only galaxy that is flagged by Fischer et al. (2019) because of a non-reliable fit and thus has no proper photometric measurements, is G24, whose spectroscopic analysis reveals the presence of two interacting galaxies, as described in Mazzilli Ciraulo et al. (2021). Therefore, we manually define this source as a merger.

3.1.2. Morphology of the DP/MaNGA galaxies

Figure 5 displays the morphology defined for the 29 DP/MaNGA galaxies. We observe that the sample is dominated by late-type galaxies (LTGs, more than 55%) and hosts 14% of merger-classified galaxies. We note that contrary to Maschmann et al. (2020), there is no significant excess of S0. This is due to the fact that the DP/MaNGA are relatively close galaxies (with a median redshift of 0.0577), while distant S0 galaxies can correspond to unresolved LTGs. One can observe that the morphology distribution of the DP/MaNGA is very close to the CS1 one.

In order to explore the morphological properties of these galaxies in greater detail, we compute the photometric parameters Gini and M_{20}, which is described in Appendix A. In Fig. A.1 we show the Gini-M_{20} diagram and observe that the sample is dominated by early-type galaxies with a large fraction of objects lying in the E-Sa region. However, we do not detect any significant difference with respect to the CS1. Maschmann et al. (2020) found a deficit of Sb-d galaxies in the DPS, composed of 5663 galaxies up to $z = 0.3$. We are here limited by the small statistics of the DP/MaNGA sample (7 galaxies are identified as Sb-Sd) and cannot be further categorised into more detailed Hubble types. Figures 3 and 4 illustrate that the morphologies of the blue-cloud and green-valley galaxies are quite diverse even though dominated by late-type ones, while the two galaxies of the red sequence are an elliptical and an S0 (see Fig. 4).

Last, Maschmann et al. (2020) showed that the DP feature is not related to the inclination of the main disc. The DP/MaNGA sub-sample is representative, with a mean inclination value of 53.5° and values distributed between 32° and 80°.
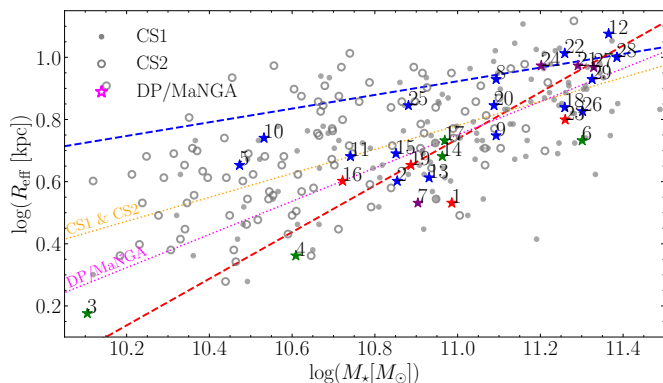
3.2. Mass-size relation and Sérsic index

Fig. 6: Size-stellar mass distribution for the DP MaNGA galaxies. The dashed lines correspond to the low-z relations proposed by van der Wel et al. (2014) ($R \propto M_\star^{0.75}$ for ETGs in red and $R \sim M_\star^{0.22}$ for LTGs in blue). The colour-coding refers to the morphology described in Sect. 3.1: ★ ellipticals, ★ S0; ★ mergers; ★ LTGs. The dotted lines refer to the relation found for the DP/MaNGA galaxies (in magenta) and based on both control samples galaxies (in orange).

Figure 6 shows the mass-size relation for the DP/MaNGA galaxies and the control samples. The stellar masses are from Salim et al. (2016), except for G7, G21 and G25 whose estimates are taken from Kauffmann et al. (2003a). The half-light radius $R_{\rm eff}$ are from the NASA-Sloan Atlas catalogue (NSA)[3]. We superimpose the low-z relations from van der Wel et al. (2014). The trend based on the CS1 and CS2 measurements, shown as an orange dotted line, lies between these two relations. For the DP/MaNGA galaxies, we observe a large scatter with the morphological types, but, while most of these galaxies are late-type galaxies, they are closer to the early-type trend ($M_\star^{0.75}$), as presented by the fitting line in magenta. This behaviour is in line with our expectations: the E-Sa galaxies are more compact than the late-type ones, at a given mass.
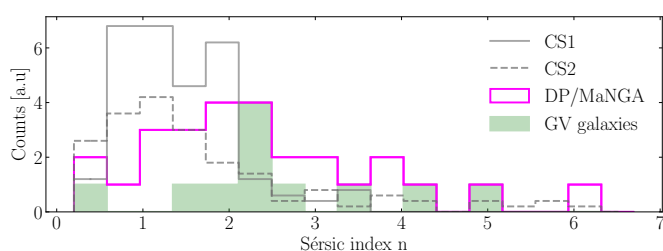
Fig. 7: Sérsic indices for the DP/MaNGA, the CS1 and the CS2 galaxies. The Sérsic indices are computed using STATMORPH for CS1 and are taken from the MaNGA PyMorph DR15 photometric catalogue for DP/MaNGA and CS2 (Fischer et al. 2019). The filled histogram corresponds to the green valley DP/MaNGA galaxies.

As discussed in Maschmann et al. (2020) for the DPS, the DP/MaNGA galaxies exhibit a higher Sérsic index than the CS1 and CS2 galaxies, as shown in Fig. 7. This further supports our finding on the mass-size relation. The DP/MaNGA galaxies are

---

relatively compact galaxies, but this effect is not detected in the morphology.

3.3. Environment

The data sets presented in Yang et al. (2007) and in Saulder et al. (2016) provide galaxy groups and enable us to know whether a galaxy is isolated or not. To discriminate from the different environments, we use the galaxy group sizes as defined in Blanton & Moustakas (2009): a poor group holds 2 to 4 objects, a rich group 5 to 9 and a cluster 10 or more. We take the classification from Saulder et al. (2016) when available and from Yang et al. (2007) for the sources with a redshift greater than 0.11. We show the environment distribution of the DP/MaNGA, the CS1 and the CS2 galaxies in Fig. 8. The DP/MaNGA galaxies are mainly isolated and in poor groups and roughly follow the distribution of the CS1/CS2 galaxies. We note a small excess (2σ, resp. 3σ) of sources without any neighbour compared to the CS1 (resp. CS2) and (resp. slightly) less objects evolving in a rich group with respect to the CS2 (resp. CS1). This result is compatible with the findings of Maschmann et al. (2020) based on 5663 DP galaxies. The bottom panel of Fig. 8 shows that
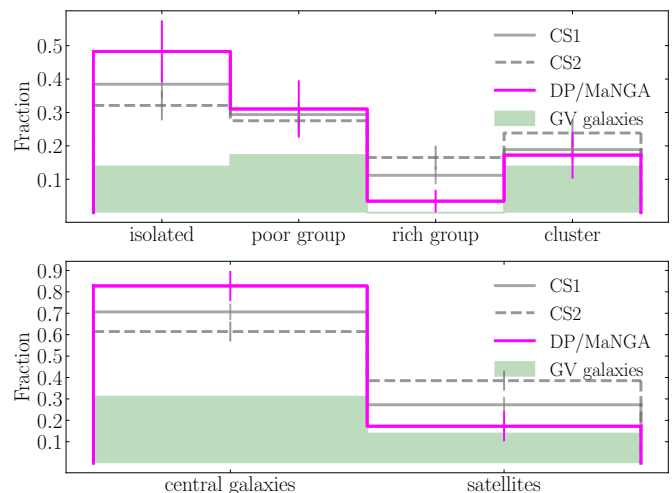

Fig. 8: **Top:** Environment distribution for the DP/MaNGA galaxies, the CS1 and the CS2 objects. The filled histogram corresponds to the green valley DP/MaNGA galaxies. The error bars show the binomial errors. **Bottom:** Distribution between central and satellite galaxies, for the DP/MaNGA, CS1 and CS2 samples. Isolated galaxies are classified as central.

most of the DP/MaNGA galaxies correspond to central galaxies of groups or clusters with a central/satellite ratio of 4.8, and that satellite DP/MaNGA galaxies are in the green-valley (except G8 which lies in the blue cloud and is in transition). This is quite different from the CS1 which has a central/satellite ratio of 2.67, and from the CS2 with a ratio of 1.60. When one considers the DPS (resp. NBCS), 17 % (resp. 9 %) of the satellite galaxies are in the green valley, supporting the fact that this excess of green satellite galaxies is real. Lastly, we note that while the central/satellite ratio in the green valley is similar for DP/MaNGA and DPS galaxies, the global DPS central/satellite ratio is of the order 2.25 independently of the redshift range (to compare with 4.8 for the DP/MaNGA).

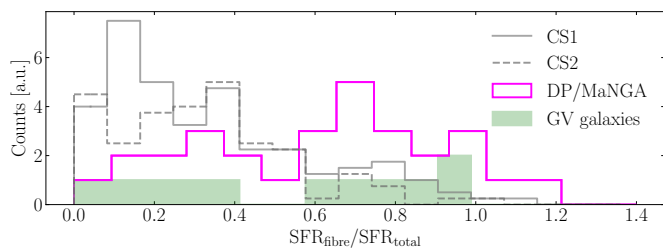## 3.4. Green valley and transition

Fig. 9: Central excess of SFR (Brinchmann et al. 2004) for the DP/MaNGA, the CS1 and the CS2 galaxies. The filled histogram corresponds to the green valley DP/MaNGA galaxies.
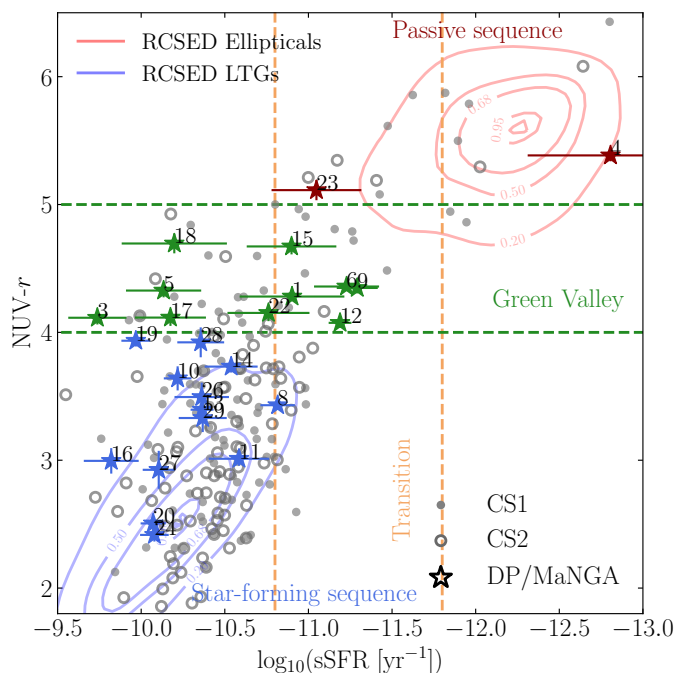

Fig. 10: NUV-*r* vs. sSFR diagram. The galaxies from the RCSED are shown as reference: the red (resp. blue) contour lines correspond to the elliptical (resp. late-type) galaxies, classified using the algorithm presented in Domínguez Sánchez et al. (2018). The transition zone represented by the two orange dashed lines is defined in Salim (2014). The CS1 objects are shown as grey dots while the DP/MaNGA are represented by coloured stars. The NUV-*r* colour, available for 25 objects, is taken from Chilingarian et al. (2017), it is dust- and k-corrected. The sSFR values are derived from SED fitting of UV and optical spectra, computed by Salim et al. (2016).

Maschmann et al. (2020) discussed that late-type DP galaxies exhibit a central enhancement of their star formation activity with respect to their control sample. We perform the same analysis by computing the ratio of the SFR computed inside the SDSS 3″ fiber SFR_{fiber} and the total SFR SFR_{total}, provided by Brinchmann et al. (2004). For the DP/MaNGA sample, we do detect a global excess of central star formation enhancement as shown in Fig. 9, but it is not possible to disentangle this effect by morphological type. However, we note that the DP/MaNGA distribution

seems bi-modal. In the following, we will further discuss this distribution that is limited here by the integration in the fibre.

Salim (2014) showed that the green-valley galaxies, defined with their NUV-*r* colour, correspond mainly to galaxies in transition with intermediate specific star formation ratio (sSFR = SFR/$M_\star$). Figure 10 displays the NUV-*r* colour with respect to the sSFR for the DP/MaNGA galaxies. The NUV magnitude comes from Galaxy Evolution Explorer (GALEX, Martin et al. 2005; Morrissey et al. 2007) and the *r* magnitude is provided by the SDSS survey. For the sSFR, we use the estimates from Salim et al. (2016) when available, and those from Brinchmann et al. (2004), for the 3 galaxies not in S16. As discussed by Salim (2014), the NUV-*r* colour defines the so-called green valley, while the $u - r$ and $g - r$ colours are more ambiguous. Four DP/MaNGA objects are lacking a NUV measurement: G25 can be classified with the other colours as clearly on the blue sequence, while G2, G7 and G21 are ambiguous, and will be later discussed.

Table 2 shows, as illustrated in Fig. 10, that 48% of the DP/MaNGA objects appear to belong to the blue cloud, while 45% lie in the green valley, but only 25% of the CS1 galaxies are green-valley galaxies. Given small number statistics, these trends are in fact not significant (1.4σ and 1.3σ respectively). However, when one considers the whole DPS catalogue from Maschmann et al. (2020), as summarised in Tab. 2, there is an excess of green-valley galaxies (a factor 2) with respect to the no-bias control sample (NBCS). Interestingly, this excess disappears when one considers the galaxies in transition with respect to their sSFR, as defined by Salim (2014) ($-11.8 < \log(sSFR) < -10.8$). Last, we note that while nearly half of the DP/MaNGA galaxies are in the green valley, only 17% of the DPS galaxies are in the green valley. This difference still stands if we consider the objects of the DPS with $z < 0.136$.

Table 2: Classification based on the colour-sSFR diagrams. The first (resp. second) part regards the DP/MaNGA sample compared to the CS1 (resp. the DPS compared to the NBCS from Maschmann et al. 2020).

	DP/MaNGA (29)		CS1 (143)	
NUV measurements	25	(86%)	115	(80%)
Blue cloud	14	(48%)	76	(66%)
Green valley	13	(45%)	29	(25%)
Red sequence	2	(7%)	10	(9%)
Transition zone	7	(27%)	22	(20%)
	DPS (5663)		NBCS (5128)	
NUV measurements	4336	(82%)	4628	(85%)
Blue cloud	3578	(63%)	3831	(75%)
Green valley	962	(17%)	410	(8%)
Red sequence	88	(2%)	95	(2%)
Transition	483	(9%)	596	(12%)

As one can notice in Fig. 10, four galaxies, namely G3, G5, G17 and G18 (and a few more discussed below), are efficiently forming stars but are situated in the GV. They are somehow reddish star-forming usually "blue" galaxies. We exclude that these galaxies are affected by undetected dust as (1) we do not see any clear excess in 22μm WISE photometry (Wide-field Infrared Survey Explorer, Wright et al. 2010), and (2) SFR estimate of Salim et al. (2016) is accounting for 22μm WISE fluxes. As we further discuss in the next section, this green feature is due to old stellar populations. However, contrarily to Belfiore et al.
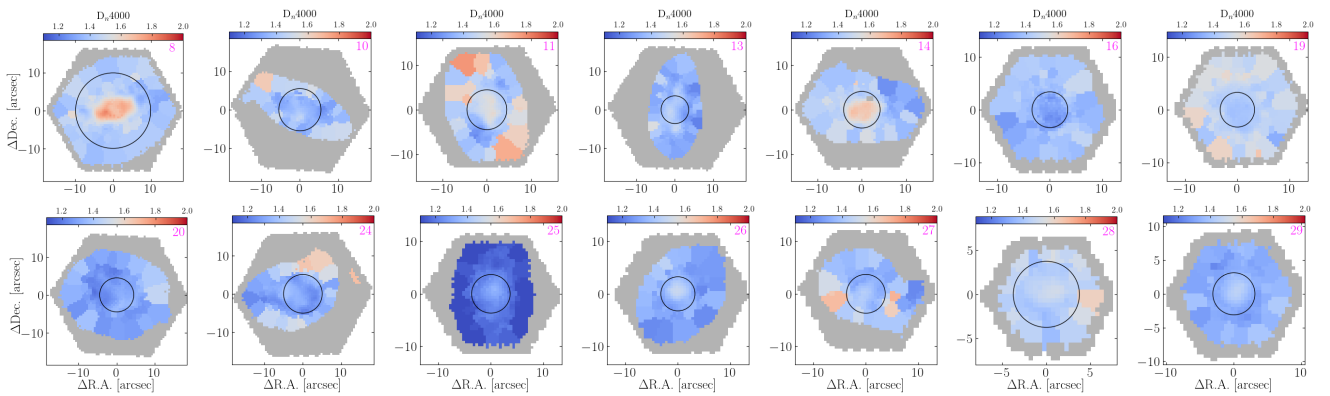
Fig. 11: D_n4000 for the DP/MaNGA galaxies of the blue cloud. The superposed circles indicate R_{eff}.
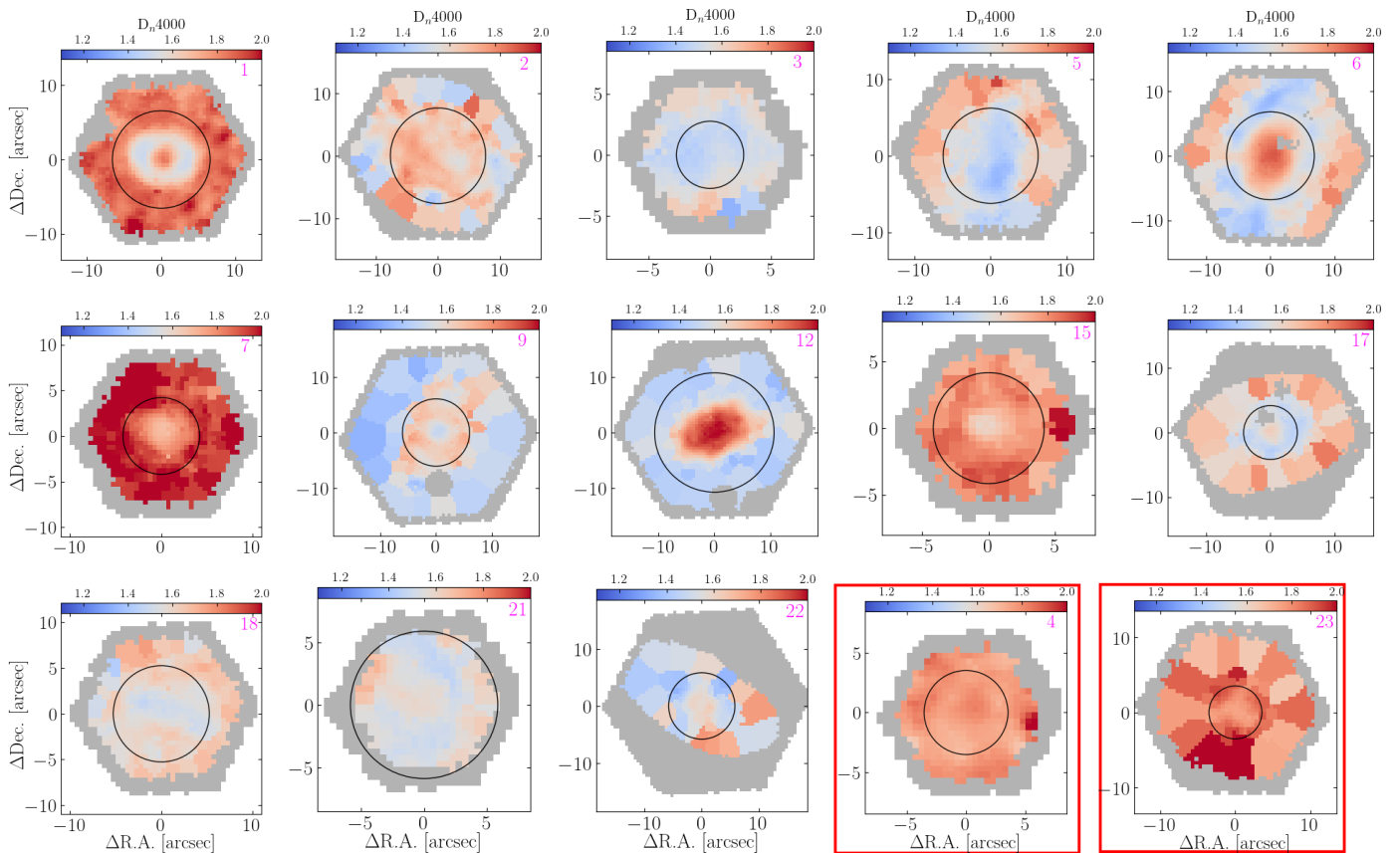

Fig. 12: Same as Fig. 11 for the green-valley and red galaxies. The red galaxies are displayed with red boxes.

(2016), these galaxies are not Low-Ionisation Emission-line Regions (LIERs) as they are actively forming stars.

3.5. Stellar indicator of age: 4000-Å break

Figures 11 and 12 display the $D_n(4000)$, discussed by Kauffmann et al. (2003b) (hereafter K03). It is defined as the ratio of the integral of the flux in the $4000 - 4100$Å range divided by the integral of the flux in the $3850 - 3950$Å range. This indicator quantifies the strength of the 4000-Å break, which traces a deficiency of hot, blue stars. As discussed by these authors, this index is proportional to the age of the stellar population. Stellar populations younger than 1 Gyr are characterised by an index $D_n(4000) < 1.5$. Figures 11 and 12 show that, while galaxies in

the blue cloud host effectively young stellar populations (on average aged of 800 Myr, traced by an average $D_n(4000)$ value of ~ 1.4), the green-valley galaxies like those of the red sequence host old stellar populations. However, they can be observed with two different $D_n(4000)$ spatial distributions: some host old stellar populations in their centre and younger outside, while others have an opposite configuration.

This index thus makes possible to further classify the ambiguous galaxies (G2, G7, G21, G25) that have no NUV measurement (as discussed in Sect. 3.4). G25 has no NUV measurement but hosts the highest SFR and the youngest stellar population of the DP/MaNGA sample. It has been classified in the blue cloud. Alternatively, G7 hosts the oldest stellar population and a moderate SFR. It has thus been classified in the GV. Al-

ternatively, G2 and G21 are less extreme, but we note that they have an average $D_n(4000)$ larger than 1.5 and a mean $H\delta_A$ index smaller than 4, suggesting a stellar population older than 1 Gy according to K03. Hence, we choose to classify them in the GV.
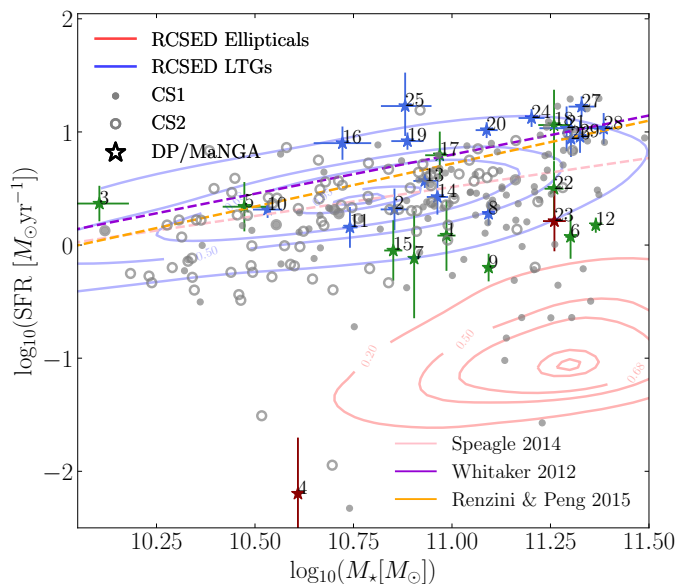

Fig. 13: SFR vs. $M_\star$ diagrams. The DP/MaNGA are represented by coloured stars. The SFR and stellar masses are based on Salim et al. (2016), except for G7, G21 and G25 (based on Brinchmann et al. 2004). The CS1 (resp. CS2) objects are shown as grey dots (resp. filled circles). The galaxies from the RCSED are shown as reference: the red (resp. blue) contour lines correspond to the elliptical (resp. late-type) galaxies, classified using the algorithm presented in Domínguez Sánchez et al. (2018).

4. Star-forming/Composite excitation and hidden AGN

In this section, we will discuss the excitation properties of the different galaxies of the DP/MaNGA sample. In Sect. 4.1, we discuss the star formation main sequence and the age of the stellar populations. In Sect. 4.2, we estimate the AGN fraction present in the DP/MaNGA galaxies. In Sect. 4.3, we study the BPT diagrams.

4.1. Star formation main sequence and stellar population age

Figure 13 displays the star-forming main sequence (SFMS, e.g. Whitaker et al. 2012; Speagle et al. 2014; Renzini & Peng 2015). The DP/MaNGA galaxies are superimposed on the RCSED distributions (80% contours) of late-type (resp. elliptical) galaxies which sample the main sequence (resp. the passive sequence). The DP/MaNGA galaxies sample the main sequence and the transition region, but exhibit a deficit of passive galaxies. The two red galaxies (as defined by their NUV-r colour) are below the SFMS, however, they are not classical quenched galaxies. On the one hand, the S0 galaxy G4 is clearly red and quenched, but shifted with respect to the location of the RCSED ellipticals in the SFR-$M_\star$ plane, due to its smaller mass. On the other hand, the elliptical galaxy G23 exhibits a star formation activity compatible with the sSFR transition zone.
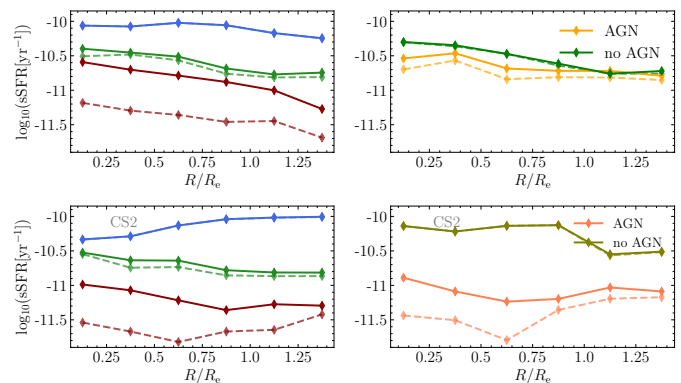
Fig. 14: Radial profiles of sSFR (SFR$_{H\alpha}/M_\star$). **Top left:** Blue, green and red median of the radial profiles. **Top right:** Radial profiles for the GV galaxies for those with a (resp. no) central AGN fraction in orange (resp. in green). The panels of the **second row** display the same radial profiles but for the CS2. The dashed lines display the sSFR values corrected for extinction and AGN's contribution. The solid lines show the sSFR values corrected for extinction only.
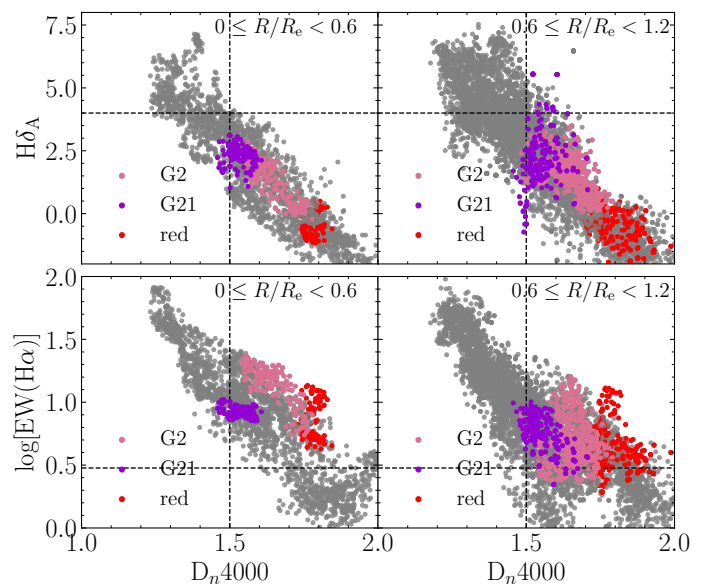

Fig. 15: Stellar age indicators for individual spaxels of the blue-cloud galaxies, represented in grey, in different radial bins. The measurements from the two red-sequence galaxies (G4 and G23) are shown as red dots. The pink (resp. violet) dots correspond to the G2 (resp. G21), ultimately classified as green-valley galaxies.

Figure 14 displays the radial behaviour of the sSFR for the blue, green and red galaxies, in the top left panel. The median profile of the galaxies belonging to the green valley is lower than that of the blue-cloud objects, and somehow less flat. This is in agreement with Belfiore et al. (2018) that found suppressed sSFR profiles for GV galaxies with respect to blue-cloud galaxies. The difference is compatible with their conclusion, as the suppression at $1.0\,R_e$ is about 0.6 dex between the blue-cloud and the GV median profiles. The **bottom** left panel displays the radial profiles of the sSFR for the CS2 galaxies. The same overall behaviour is observed but the blue galaxies exhibit a small central deficit of sSFR. Also the red galaxies profile is closer to the

green valley one for the DP/MaNGA galaxies. As discussed earlier the DP/MaNGA red galaxies are atypical, and are not well represented by the CS2 galaxies.

The right panels of Fig. 14 shows the green valley itself where we separate the radial profiles for the galaxies with or without a central AGN signature. The group with a nuclear AGN-like activity has a weaker sSFR than the one with no nuclear activity. For the DP/MaNGA galaxies, the difference is relatively small (~ 0.2 dex), while it is much larger for the CS2 galaxies (~ 1 dex). Even though we are dealing with small number statistics, such a difference is a signature that we are observing different phase of the central activity. Indeed the radial profiles of the green-valley galaxies with a central AGN activity are close to the profiles of the red galaxies.

Relying on the resolved power of the MaNGA data, we further explore the different properties of these DP/MaNGA to try to understand the quenching mechanism in the studied sources. Figure 15 displays the various stellar population age indicators
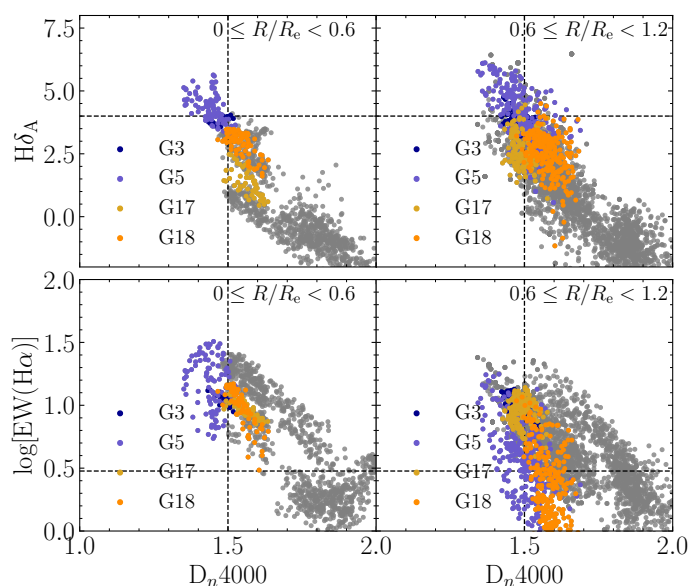
Fig. 16: Stellar age indicators for individual spaxels, of the green-valley galaxies, in different radial bins (but for G2 and G21 that are displayed in Fig. 15). The coloured points correspond to the galaxies G3, G5, G17 and G18 that have green NUV-r colour, but a high star formation activity as shown in Fig. 10.

for 2 radial bins for the blue and red galaxies. We display the Hδ_A index, based on the absorption line feature, and the equivalent width of Hα with respect to the D$_n$(4000) index. Following Kauffmann et al. (2003b), we consider that galaxies with an index Hδ_A < 4 and D$_n$(4000) > 1.5 host stellar populations older than 1 Gyr. We inspect the radial profiles of different properties of the blue-cloud galaxies. Their EW(Hα) values are mainly above 3 Å at all galactic radii. The D$_n$(4000) profiles are principally flat too, with low values typical typical of young stellar populations. Figure 15 shows that most of the red-sequence galaxies host stellar populations older than 1 Gyr, but with an EW(Hα) larger than 3 Å (excluding "retired" or passive stellar populations, as discussed in Cid Fernandes et al. 2011). Interestingly, in the blue galaxies, as shown in Fig. 11, the old stellar populations are present in the inner parts of galaxies G8, G11 and G14. G8 is a late-type galaxy in the sSFR transition zone (in Fig. 10), while the two other galaxies are late-type (G11) and

S0 (G14) with more regular profiles. Lastly, the galaxies G2 and G21, superimposed on Fig. 15, host old stellar populations and are further classified as GV galaxies (in Fig. 17 and beyond).

Figure 16 displays the same stellar parameters as Fig. 15, but for the green-valley galaxies. Contrarily to the blue galaxies, these galaxies host a significant fraction of old stellar population at all scales, as displayed in Fig. 12. We highlight four green-valley galaxies in Fig. 16 which have young stellar populations in their centre and older ones in the outer parts. Among the other galaxies, three of them (G1, G7 and G15) host old stellar population in their outer parts with EW(Hα) larger than 3Å. Two galaxies (G6 and G12) host old stellar populations in their centre, with a large EW(Hα). Lastly, the galaxies G9 and G22 are intermediate galaxies with rather old stellar population and EW(Hα) larger than 3Å in their centre.

We also look at the radial profiles of the Balmer decrement, Hα/Hβ, for all the DP/MaNGA, in order to estimate the amount of dust within these galaxies. The profiles are either flat or slightly decreasing towards outer radii, without any clear discrepancy between blue, green and red galaxies.

We conclude that, besides the small size of the DP/MaNGA sample, we observe significant trends. The green valley DP/MaNGA galaxies are galaxies with a red excess in their spectra, that is due to their stellar populations. However, one part of these galaxies have a older central stellar population, and the other part has a younger central stellar population. Some blue galaxies (like G8) have a small red excess in their central part, which does not dominate their overall colour. In parallel, red galaxies (like G23) still host star formation in a transition regime. In the subsequent section, we study how this relates to the central engine. Due to their central gas content, we do not observe any LIERs (Belfiore et al. 2016).

4.2. Resolved AGN fraction in the gas excitation

In this Section, we study the AGN fraction per spaxel, and how this AGN fraction varies with radius for the different galaxies. This enables to classify two types of green-valley galaxies. We then recomputed the central star formation excess within the (half-)central effective radius.

AGN fraction from the ionised gas emission lines

Optical emission lines can be excited by the radiation of star forming regions, but also by AGN radiation, or through shocks. Diagnostics based on line ratios such as [NII]/Hα and [OIII]/Hβ are widely used, since independent of extinction (Baldwin et al. 1981). With MaNGA data, we can estimate the fraction of AGN-dominated excitation for each spaxel.

The Hα emission is a tracer of young, hot stars, and therefore of star-formation activity, but is also contaminated by AGN's narrow line region. The observed Hα flux is thus over-estimating the SFR. Jin et al. (2021) proposed an approach to correct for the AGN's contamination in the Hα emission that we follow. We compute the AGN fraction f_{AGN}, based on the emission flux measurements provided by the DAP, that corresponds to the AGN's contribution to the Hα flux (Jin et al. 2021). Following the 3D diagnostic diagram presented in Ji & Yan (2020), the P_1 indicator is computed as:

$$P_1 = 0.63 \log([\text{NII}]/\text{H}\alpha) + 0.51 \log([\text{SII}]/\text{H}\alpha)$$
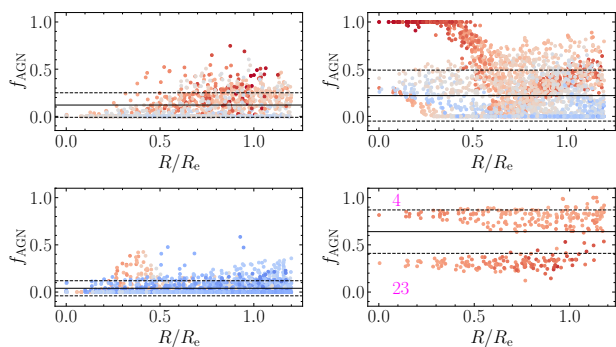$$+ 0.59 \log([\text{OIII}]/\text{H}\beta) \qquad (2)$$

Fig. 17: Spaxel-by-spaxel radial profiles of the AGN fraction f_{AGN} for the DP/MaNGA galaxies. Each panel corresponds to different types of galaxies defined in the colour-sSFR diagram in Fig. 10. The top panels display the GV galaxies, the left (resp. right) panel shows the profiles of the objects without (resp. with) any important AGN fraction in their inner parts. The bottom left (resp. right) panel displays the blue (resp. red) galaxies. The dots are colour-coded with the $D_n(4000)$ values, shown on Figs 11 and 12. The full (resp. dashed) lines refer to the averaged (resp. rms) values $\langle f_{AGN} \rangle$ and σ_{AGN} computed following Eq. B.1 and listed in Tab. B.1.

Then, the AGN fraction is set such that:

$$
f_{AGN} = \begin{cases} 0 & \text{if } P_1 \leq -0.53 \\ 0.14 P_1^2 + 0.96 P_1 + 0.47 & \text{if } -0.53 < P_1 \leq 0.51 \\ 1 & \text{if } P_1 \geq 0.51 \end{cases}
$$

(3)

In this way, the AGN fraction is a number such that $0 < f_{AGN} < 1$, depending on the value of P_1. This relation was applied to all spaxels where all the lines have a reliable emission (S/N > 3) in the emission lines required for the P_1 parameter computation. Figures B.1 and B.2 show the resulting 2D maps of the f_{AGN} value for all the DP/MaNGA galaxies. Figure 17 displays radial profiles of the f_{AGN} fraction of the DP/MaNGA galaxies. In the bottom panels corresponding to the blue (left) and red (right) galaxies, the radial profiles are flat, but differs by the level. As discussed in Jin et al. (2021), the blue galaxies have no significant central AGN fraction, contrarily to the red galaxies. The radial profiles of the AGN fraction f_{AGN} are flat for the blue galaxies (and null) but for the galaxy in transition (8), and for a few that exhibit weak f_{AGN} in their disc. They are also flat for the red galaxies (but at a value of about 0.8 (G4) and 0.3 (G23)). Alternatively, for the GV galaxies, we note two types of behaviours: the galaxies with a nuclear activity and those with none. The top panels of Fig. 17 display the spaxel-based resolved profiles of these two types of galaxies: the GV galaxies with no AGN fraction in their centre (G2, G3, G7, G15, G17, G18, G21), and the GV galaxies with non-zero AGN fraction in their centre (G1, G5, G6, G9, G12, G22). The former category exhibits a behaviour close to the one of the blue category. The latter shows high and medium levels of AGN fraction in their centre, but contrarily to the red galaxies the radial profiles are not flat. They seem in an multi-stage transition regime, resulting in the composite excitation observed in the BPT diagram (see below). All the four panels show a correlation between the AGN fraction f_{AGN} and the $D_n(4000)$ index: the AGN fraction is low for low $D_n(4000)$ values, tracing young stellar populations. Higher values of f_{AGN} are characterised by greater $D_n(4000)$.

Figure 17 displays the mean and scatter (rms) for each panel. This is further discussed in Appendix B. We clearly observe that the means are systematically smaller for the non-central-AGN galaxies than for the central-AGN galaxies. When this AGN fraction is used to correct the sSFR, the radial profiles displayed in Fig. 14 decrease by 0.5 dex for the red galaxies and the green-valley galaxies of the CS2, while the effect is smaller (~ 0.1 dex) for the green valley DP/MaNGA galaxies, while the green valley BPT are less filled due to small statistics.
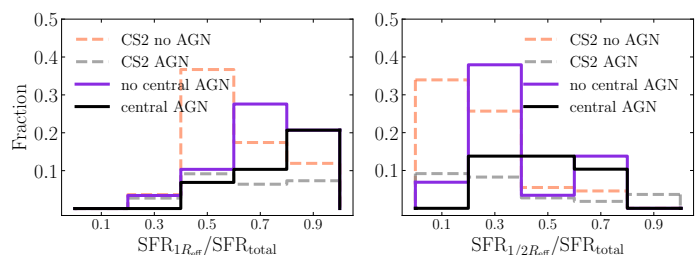
Central star formation excess

Fig. 18: Star-formation excess computed within an elliptical radius of R_{eff} (left) and $0.5 R_{eff}$ (right). The DP/MaNGA galaxies with and without nuclear activity are compared with their counterparts from the CS2 control sample.

Figure 18 displays the central star formation excess computed within radii of $0.5 R_{eff}$ and $1.0 R_{eff}$, for DP/MaNGA and CS2 galaxies. This excess is given as fractions for objects with and without a central AGN activity. It shows that the area over $1 R_{eff}$ contains at least 50% of the Hα-based star formation rate of the galaxies. The fractions are systematically lower for the CS2 sample. The right panel displays the same systematic central SF excess for the DP/MaNGA galaxies with respect to the CS2 ones but shows that the star formation activity is not restricted to the nucleus but distributed within the effective radius. In parallel, there is no clear effect between the central and satellite galaxies.

4.3. Resolved BPT diagrams

Figure 19 displays the BPT diagrams for the same categories of galaxies displayed in Fig. 17. The red galaxies lies at the border of the composite region, but mainly with the Seyfert and LINER classifications (and we discussed previously that they are not LIERs based on Fig. 15). The blue galaxies are star-forming in their centre with some spaxels from composite excitation in their outskirts (e.g. galaxy 8, which has a profile close to the upper left panel). The GV galaxies have been separated into two categories based on their AGN fraction. They mostly present a BPT diagram with spaxels along the diagonal, i.e. different from the blue galaxies. The green-valley galaxies with a central fraction of AGN have spaxels located further towards the Seyfert/LINER regions than their green with no central-AGN-fraction counterparts. The difference of the spatially-resolved BPT shape between the latter and the one of the blue-cloud objects suggests that the GV galaxies are moving from the star-formation regime to the composite one. The four emission lines used in this diagnostic diagram are required to reach a minimal signal-to-noise ratio of 3, so the lower number of detected spaxels away from the galaxy centre (displayed in red on Fig. 19) can be caused by a lack of ionised gas at the large radii. But this is also to be accounted for the spatial coverage of the MaNGA, which is either
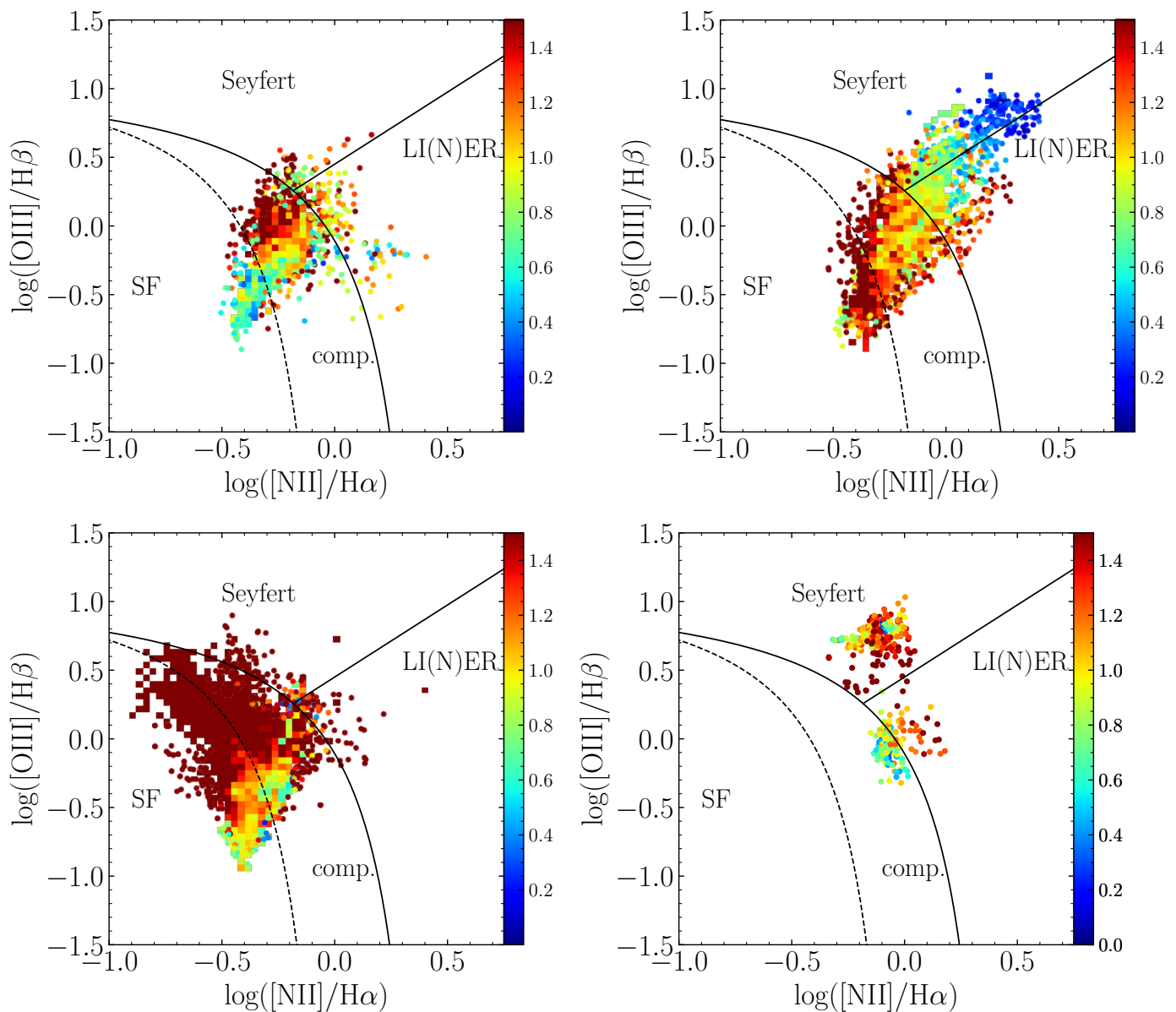
Fig. 19: BPT diagrams. **Top panels:** Green valley galaxies with a (resp. no) central AGN fraction on the right (resp. left). **Bottom-left panel:** Blue-sequence galaxies. **Bottom-right panel:** Red-sequence galaxies. The colour indicates the distance to the center, in units of R_e.

out to $1.5R_{\rm eff}$ or $2.5_{\rm eff}$ (Wake et al. 2017) and in our case, the majority of the blue-cloud galaxies are covered to $2.5R_{\rm eff}$ while most of the green-valley objects are covered to $1.5R_{\rm eff}$. The BPT diagrams for the CS2 galaxies, following the same group division, are shown in Fig. C.1. In general, the spaxel distributions follow the same trends as for those of the DP/MaNGA galaxies, while the BPT diagrams corresponding to the green-valley galaxies are less filled due to small statistics. We also note that the CS2 red galaxies are better sampling the BPT, with a non-negligible component of star-forming regions in the outskirt.

4.4. Summary

The DP galaxies from Maschmann et al. (2020) are characterised by an excess of GV galaxies (defined with their NUV-r colour) with respect to the no-bias-control sample. We have studied the DP/MaNGA galaxies among the DP sources and found that for

these sources the red-excess of the GV galaxies is due to their stellar population (with the $D_n(4000)$ index). A fraction of these galaxies are actively star-forming, while the others are in the transition zone of star formation. We identified two types of GV galaxies, those with a high AGN fraction in their centre, and the others with no AGN fraction in their centre. The latter have a positive $D_n(4000)$ gradient, while the former exhibit a negative one. This sample is quite peculiar in the sense that the selection has been somehow based on star-forming galaxies (i.e. with detectable emission lines) and green-valley galaxies. It thus enables to study on-going quenching mechanisms.

5. Discussion

In this section, we discuss how the DP/MaNGA galaxies fit into the more general context of galaxy quenching. In Sect. 5.1, we discuss the scenario of inside-out quenching, then in Sect. 5.2

outside-in. In Sect. 5.3, we compare the compatibility of our new findings with the scenario of minor mergers accounting for the central SFR excess and the large bulge features.

5.1. Quenching inside-out

The GV galaxies are redder that their blue counterparts as they host redder stellar populations. On the BPT, they host obvious signs of AGN-related emission in their centre for a fraction of them, clearly in transition. Those galaxies host old stellar populations in their centre, but the EW(Hα) is there larger than 3Å, excluding the LIER stage, excited only by old stars, without any young star formation, nor any nuclear activity at the origin of their excitation, described by Belfiore et al. (2017). The other part of the GV galaxies host younger stellar populations in their centre, but their location on the BPT diagram seems intermediate between the blue galaxies and the former GV galaxies, suggesting an underlying nuclear activity. This scenario would be in agreement with the results of Bluck et al. (2020a,b) based on the exploitation of spatially resolved star formation rates of MaNGA galaxies. Beside the evidence of nuclear activity, these authors also discussed that central galaxies preferentially quench inside-out, while our DP/MaNGA galaxies are mainly isolated or in small groups, they are hence mainly centrals.

Various studies have questioned the correlation between AGN and the quenching mechanism (McPartland et al. 2019; Chen et al. 2020). Our work shows that nuclear activity can be weak and escape detection. This kind of nuclear activity would certainly be undetected at high-z. Our results are in good agreement with Barrows et al. (2017), who found the AGN triggering is more probable at late-merger stages.

5.2. Quenching outside-in

Alternatively, green-valley galaxies that are actively forming stars with no-central AGN fraction and hence undetected nuclear activity host blue central stellar populations and red stellar populations in their outskirts. Some of these DP/MaNGA galaxies (including some blue ones) are quenched in their outskirts as displayed in Fig. 15 and 16. They could have quenched their outskirt star-formation activity either by environment or gas exhaustion, as discussed in Peng et al. (2010) (see also Schawinski et al. 2014).

The $D_n(4000)$ stellar population index traces the relatively young stellar populations in different massive galaxies whose masses are dominated by the old stellar population. These intermediate galaxies might host slightly less gas and star formation than the others. Could they be old galaxies having accreted gas in their centre and possibly triggering weak nuclear activity? Relying on SDSS galaxies, Kaviraj (2014) discussed that disturbed spirals also exhibit higher nuclear-accretion rates, and they interpret this with minor mergers, which can represent 40% of star formation in spirals.

Last, it is also possible that the underlying nuclear activity (detected in Fig. 19) has changed in intensity with time and generated turbulence which might impact the velocity dispersion (and the DP feature) and the star-formation. Mandal et al. (2021) studied with simulations the interaction of the interstellar medium with the radio jet. They found that the dense clouds near the central region, where the density is enhanced due to the compression, exhibit a generally higher SFR than the clouds in the outskirts, even though lower than with no-jet counterparts. This study is focused on the case where the jet lies in the disc, while

there is no radio jet detection in DP/MaNGA galaxies characterised by a weak nuclear activity.

5.3. Minor mergers and other alternatives

The DP galaxies are characterised by a larger Sérsic index than the control samples matched in stellar mass and redshift, as well as by a central star formation rate excess. While classical bulges are thought to be built through mergers (e.g. Weinzirl et al. 2009), with some violent processes followed by strong relaxation (see also Mihos & Hernquist 1994), a bulge growth is also expected in the multiple sequential merger scenario proposed by Bournaud et al. (2007). The DP/MaNGA galaxies also correspond to the trend discussed in Lotz et al. (2008): post-coalescence galaxies are more concentrated in their light distribution, while tidal features vanish. In parallel, Martig et al. (2013) claimed that only a few amounts of gas can be stabilised against star formation in galaxies with massive spheroids (the so-called morphological quenching). Indeed, high surface densities can allow the gas to fragment. Moreover, interactions with other galaxies can trigger star formation, and, in these cases, some early-type galaxies are not completely quenched. This concentration can also be observed for bar-driven gas infall (e.g. Schinnerer et al. 2007; Kim & Elmegreen 2017). However, there is only a small fraction of barred objects in the DP/MaNGA sample (about 17% according to the photometric value-added catalogue) and the spatial resolution is not adapted to detect inner bars, but we cannot exclude at this stage that the DP feature is due to a decoupled inner kinematic structure.

Interestingly, Kaviraj et al. (2009) discussed that merger events onto early-type galaxies could account for red NUV-r colour. They claim that an intermediate NUV-r colour, as observed for 7 out of the 9 early-type DP/MaNGA galaxies, can result from minor mergers with smaller mass ratios than 1:6 or from mergers with higher mass ratios but more than $\sim$ 1Gyr old. On the other hand, early-types with bluer colour (NUV-r < 3.8, as galaxies G14 and G16) can originate from mergers with mass ratios between 1:4 and 1:6, involving progenitors with gas fractions greater than $\sim$ 20 percent.

Mancini et al. (2019) discussed that part of the green-valley galaxies could be quenched galaxies that are rejuvenated. This is supported by the observations of old bulges surrounded by young discs at $z \geq 0.5 - 1$, as well as local galaxies like M31 (Williams et al. 2017; Telford et al. 2019). Similarly, Sachdeva & Saha (2018) discussed that some bulges at $z < 1$ are bright and compact with 1.5-2 **times** larger sSFR and 2.5-6 times more massive than classical and pseudo-bulges. They discussed that these bright compact bulges could correspond to rejuvenation of existing spheroids, while the majority (80%) is old and red. This could indeed account for our observations as the $D_n(4000)$ is tracing the age of the stellar populations, but does not necessary trace the mass, while the spectral flux is dominated by the young stars.

Our results are compatible with the finding of Mountrichas et al. (2021), based on X-ray measurements who discussed a scenario where AGN and star formation are both fed by cold gas, supplied by a merger event. They found that the SFR is enhanced by 40% in presence of AGN (See also Torbaniuk et al. 2021).

6. Conclusion

We have studied the star formation and AGN properties of a sample of Double-Peaked galaxies selected from the Sloan Survey, and mapped in the MaNGA (Mapping Nearby Galaxies at

APO) survey. With these resolved maps, we obtained 2D diagnostics of AGN and/or star formation excitation of the ionised gas lines, and compared with stellar population ages, deduced from $D_n(4000)$ and $H\delta_A$ indices, colours and magnitudes. This enables us to compare the possible sources of quenching, supernovae or AGN feedback, mass or environment in DP-galaxies with respect to the control sample of single-peaked ones.

Our main results are that the DP/MaNGA galaxies have:

– a higher fraction of green-valley objects
– a green colour in the GV category due to red stellar population (hence older than 1Gyr)
– an AGN fraction linked to the stellar population age
– more than 50% of the star formation activity occurs inside one effective radius, and is more concentrated than for galaxies of the control samples
– the galaxies are central galaxies mainly isolated or in small groups.

We can state that the different sub-groups defined in this analysis constitute an evolutionary sequence. The blue-cloud galaxies exhibit star-forming discs with an important gas content and a star formation concentrated in their inner parts, compatible with gas accretion through minor mergers. In these mergers, the gas may come in part from the companion, but the major part from the gas reservoir of the primary galaxy's outskirts, which is depleted and driven inwards by the interaction. After the central star formation has faded, the gas fuels the central engine of these objects, triggering a nuclear activity supposed linked to weak AGN, even though we cannot exclude intense star formation and associated feedback. AGN-like signatures are then observed, linked with old stellar populations in the central regions, and the galaxy enters the green valley. The nuclear activity of these GV galaxies is then observed to reduce the central star formation (inside-out quenching). In a possible next phase, the gas from the disc infalls and fuels again the central region, but the disc is no longer replenished from the depleted outer reservoir. The disk appears then quenched outside-in. These two transitions are mainly observed in the green-valley galaxies, which are observed in excess in the DP galaxy population.

In forthcoming papers, we will continue the investigation of the double-peaked MaNGA galaxies through other properties such as their old gas content using CO and HI observations to further explore the quenching mechanisms involved and their kinematics using a multi-component analysis to interpret their global evolution.

References

Aguado, D. S., Ahumada, R., Almeida, A., et al. 2019, ApJS, 240, 23
Baldry, I. K., Glazebrook, K., Brinkmann, J., et al. 2004, ApJ, 600, 681
Baldwin, J. A., Phillips, M. M., & Terlevich, R. 1981, PASP, 93, 5
Barrows, R. S., Comerford, J. M., Zakamska, N. L., & Cooper, M. C. 2017, ApJ, 850, 27
Belfiore, F., Maiolino, R., Bundy, K., et al. 2018, MNRAS, 477, 3014
Belfiore, F., Maiolino, R., Maraston, C., et al. 2017, MNRAS, 466, 2570
Belfiore, F., Maiolino, R., Maraston, C., et al. 2016, MNRAS, 461, 3111
Blanton, M. R., Bershady, M. A., Abolfathi, B., et al. 2017, AJ, 154, 28
Blanton, M. R., Kazin, E., Muna, D., Weaver, B. A., & Price-Whelan, A. 2011, AJ, 142, 31
Blanton, M. R. & Moustakas, J. 2009, ARA&A, 47, 159
Bluck, A. F. L., Maiolino, R., Piotrowska, J. M., et al. 2020a, MNRAS, 499, 230
Bluck, A. F. L., Maiolino, R., Sánchez, S. F., et al. 2020b, MNRAS, 492, 96
Boselli, A., Cuillandre, J. C., Fossati, M., et al. 2016, A&A, 587, A68
Bournaud, F., Jog, C. J., & Combes, F. 2007, A&A, 476, 1179
Brinchmann, J., Charlot, S., White, S. D. M., et al. 2004, MNRAS, 351, 1151
Bundy, K., Bershady, M. A., Law, D. R., et al. 2015, ApJ, 798, 7
Cappellari, M. 2017, MNRAS, 466, 798
Cappellari, M. & Emsellem, E. 2004, PASP, 116, 138
Chabrier, G. 2003, PASP, 115, 763
Chen, Z., Faber, S. M., Koo, D. C., et al. 2020, ApJ, 897, 102
Chilingarian, I. V., Zolotukhin, I. Y., Katkov, I. Y., et al. 2017, ApJS, 228, 14
Cid Fernandes, R., Stasińska, G., Mateus, A., & Vale Asari, N. 2011, MNRAS, 413, 1687
Coenda, V., Martínez, H. J., & Muriel, H. 2018, MNRAS, 473, 5617
Comerford, J. M., Gerke, B. F., Stern, D., et al. 2012, ApJ, 753, 42
Comerford, J. M., Nevin, R., Stemo, A., et al. 2018, ApJ, 867, 66
Condon, J. J., Helou, G., Sanders, D. B., & Soifer, B. T. 1993, AJ, 105, 1730
Dey, A., Schlegel, D. J., Lang, D., et al. 2019, AJ, 157, 168
Di Matteo, P., Bournaud, F., Martig, M., et al. 2008, A&A, 492, 31
Domínguez Sánchez, H., Huertas-Company, M., Bernardi, M., Tuccillo, D., & Fischer, J. L. 2018, MNRAS, 476, 3661
Drory, N., MacDonald, N., Bershady, M. A., et al. 2015, AJ, 149, 77
Falcón-Barroso, J., Sánchez-Blázquez, P., Vazdekis, A., et al. 2011, A&A, 532, A95
Fischer, J. L., Domínguez Sánchez, H., & Bernardi, M. 2019, MNRAS, 483, 2057
Ge, J.-Q., Hu, C., Wang, J.-M., Bai, J.-M., & Zhang, S. 2012, ApJS, 201, 31
Holmberg, E. 1958, Meddelanden fran Lunds Astronomiska Observatorium Serie II, 136, 1
Inami, H., Armus, L., Surace, J. A., et al. 2010, AJ, 140, 63
Ji, X. & Yan, R. 2020, MNRAS, 499, 5749
Jin, G., Dai, Y. S., Pan, H.-A., et al. 2021, arXiv e-prints, arXiv:2109.11084
Kauffmann, G., Heckman, T. M., White, S. D. M., et al. 2003a, MNRAS, 341, 33
Kauffmann, G., Heckman, T. M., White, S. D. M., et al. 2003b, MNRAS, 341, 54
Kaviraj, S. 2014, MNRAS, 440, 2944
Kaviraj, S., Peirani, S., Khochfar, S., Silk, J., & Kay, S. 2009, MNRAS, 394, 1713
Kaviraj, S., Shabala, S. S., Deller, A. T., & Middelberg, E. 2015, MNRAS, 452, 774
Kim, W.-T. & Elmegreen, B. G. 2017, ApJ, 841, L4
Kroupa, P. 2001, MNRAS, 322, 231
Lahén, N., Johansson, P. H., Rantala, A., Naab, T., & Frigo, M. 2018, MNRAS, 475, 3934
Law, D. R., Cherinka, B., Yan, R., et al. 2016, AJ, 152, 83
Lotz, J. M., Davis, M., Faber, S. M., et al. 2008, ApJ, 672, 177
Lotz, J. M., Primack, J., & Madau, P. 2004, AJ, 128, 163

Mancini, C., Daddi, E., Juneau, S., et al. 2019, MNRAS, 489, 1265
Mandal, A., Mukherjee, D., Federrath, C., et al. 2021, MNRAS, 508, 4738
Martig, M., Bournaud, F., Teyssier, R., & Dekel, A. 2009, ApJ, 707, 250
Martig, M., Crocker, A. F., Bournaud, F., et al. 2013, MNRAS, 432, 1914
Martin, D. C., Fanson, J., Schiminovich, D., et al. 2005, ApJ, 619, L1
Maschmann, D. & Melchior, A.-L. 2019, A&A, 627, L3
Maschmann, D., Melchior, A.-L., Mamon, G. A., Chilingarian, I. V., & Katkov, I. Y. 2020, A&A, 641, A171
Mazzilli Ciraulo, B., Melchior, A.-L., Maschmann, D., et al. 2021, A&A, 653, A47
McPartland, C., Sanders, D. B., Kewley, L. J., & Leslie, S. K. 2019, MNRAS, 482, L129
Meert, A., Vikram, V., & Bernardi, M. 2015, MNRAS, 446, 3943
Mihos, J. C. & Hernquist, L. 1994, ApJ, 431, L9
Morrissey, P., Conrow, T., Barlow, T. A., et al. 2007, ApJS, 173, 682
Mountrichas, G., Buat, V., Yang, G., et al. 2021, A&A, 653, A74
Nevin, R., Comerford, J. M., Müller-Sánchez, F., Barrows, R., & Cooper, M. C. 2018, MNRAS, 473, 2160
Patton, D. R., Ellison, S. L., Simard, L., McConnachie, A. W., & Mendel, J. T. 2011, MNRAS, 412, 591
Peng, Y.-j., Lilly, S. J., Kovač, K., et al. 2010, ApJ, 721, 193
Rasmussen, J., Ponman, T. J., Verdes-Montenegro, L., Yun, M. S., & Borthakur, S. 2008, MNRAS, 388, 1245
Renzini, A. & Peng, Y.-j. 2015, ApJ, 801, L29
Rodriguez-Gomez, V., Snyder, G. F., Lotz, J. M., et al. 2019, MNRAS, 483, 4140
Sachdeva, S. & Saha, K. 2018, MNRAS, 478, 41
Saintonge, A., Kauffmann, G., Wang, J., et al. 2011, MNRAS, 415, 61
Salim, S. 2014, Serbian Astronomical Journal, 189, 1
Salim, S., Lee, J. C., Janowiecki, S., et al. 2016, ApJS, 227, 2
Sánchez, S. F., Avila-Reese, V., Hernandez-Toledo, H., et al. 2018, Rev. Mexicana Astron. Astrofis., 54, 217
Sánchez, S. F., Pérez, E., Sánchez-Blázquez, P., et al. 2016a, Rev. Mexicana Astron. Astrofis., 52, 171
Sánchez, S. F., Pérez, E., Sánchez-Blázquez, P., et al. 2016b, Rev. Mexicana Astron. Astrofis., 52, 21
Saulder, C., van Kampen, E., Chilingarian, I. V., Mieske, S., & Zeilinger, W. W. 2016, A&A, 596, A14
Schawinski, K., Urry, C. M., Simmons, B. D., et al. 2014, MNRAS, 440, 889
Schinnerer, E., Böker, T., Emsellem, E., & Downes, D. 2007, A&A, 462, L27
Speagle, J. S., Steinhardt, C. L., Capak, P. L., & Silverman, J. D. 2014, ApJS, 214, 15
Telford, O. G., Werk, J. K., Dalcanton, J. J., & Williams, B. F. 2019, ApJ, 877, 120
Torbaniuk, O., Paolillo, M., Carrera, F., et al. 2021, MNRAS, 506, 2619
van der Wel, A., Franx, M., van Dokkum, P. G., et al. 2014, ApJ, 788, 28
Wake, D. A., Bundy, K., Diamond-Stanic, A. M., et al. 2017, AJ, 154, 86
Weinmann, S. M., Kauffmann, G., van den Bosch, F. C., et al. 2009, MNRAS, 394, 1213
Weinzirl, T., Jogee, S., Khochfar, S., Burkert, A., & Kormendy, J. 2009, ApJ, 696, 411
Westfall, K. B., Cappellari, M., Bershady, M. A., et al. 2019, AJ, 158, 231
Whitaker, K. E., van Dokkum, P. G., Brammer, G., & Franx, M. 2012, ApJ, 754, L29
Whitmore, B. C., Brogan, C., Chandar, R., et al. 2014, ApJ, 795, 156
Williams, B. F., Dolphin, A. E., Dalcanton, J. J., et al. 2017, ApJ, 846, 145
Wright, E. L., Eisenhardt, P. R. M., Mainzer, A. K., et al. 2010, AJ, 140, 1868
Wyder, T. K., Martin, D. C., Schiminovich, D., et al. 2007, ApJS, 173, 293
Yang, X., Mo, H. J., van den Bosch, F. C., et al. 2007, ApJ, 671, 153

Appendix A: Gini-M_{20} diagram

Using the python package STATMORPH[4] on the r-band Legacy survey snapshots, we calculate non-parametric morphological diagnostics (see Rodriguez-Gomez et al. 2019) in order to display our galaxies on the $G - M_{20}$ diagram (Lotz et al. 2004, 2008). This approach is based on the measurements of two parameters: the Gini coefficient G and the second-order moment of the brightest 20% of the galaxy's flux. The former can be used to quantify galaxy morphology.
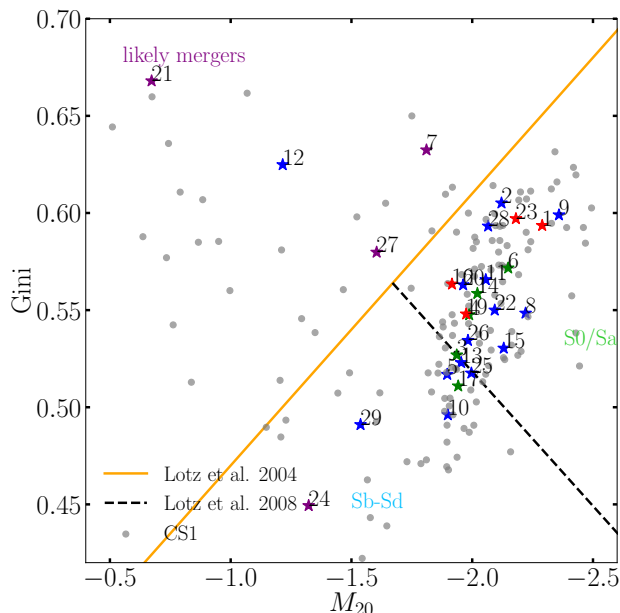

Fig. A.1: Gini vs M_{20} diagram**, based on the r-band Legacy survey image**. The CS galaxies are shown by grey dots. The orange line sets the division between merger candidates and normal Hubble types (Lotz et al. 2004). The black dotted line separates early-type (E, S0 and Sa) from late-type objects (Sb to Sd, as well as Irr) (Lotz et al. 2008). Galaxy 18 does not appear on this panel but has (-1.21,0.86) for coordinates, so falls in the "likely mergers" region.

.

In Fig. A.1, we display the so-called Gini-M_{20} diagram for the 29 DP/MaNGA galaxies, while Tab. A.1 summarises the classification of the 29 DP/MaNGA galaxies (resp. 143 CS1 galaxies) with reliable measurements.

Table A.1: Classification of the DP/MaNGA sample (coloured symbols) compared to the CS1 (grey symbols), based on the Gini-M_{20} diagram. The DP/MaNGA galaxies are colour-coded with the

	DP/MaNGA		CS	
Sb-Sd	7	(24%)	35	(24%)
S0/Sa	11	(38%)	47	(33%)
likely mergers	3	(10%)	14	(10%)

Notes: For the percentage computation, we only consider the number of galaxies that have reliable morphological measurements (see first row of the table).

---

[4] https://pypi.org/project/statmorph/

Appendix B: Averaged trends depending on galaxy colours

We estimate an averaged AGN fraction $\langle f_{AGN} \rangle$, an rms σ_{AGN} and an error ϵ_{AGN} of this quantity for each of the four galaxy types:

$$\langle f_{AGN} \rangle = \frac{\Sigma \phi_{H\alpha} f_{AGN}}{\Sigma \phi_{H\alpha}}; \sigma_{AGN} = \sqrt{\langle f_{AGN}^2 \rangle - \langle f_{AGN} \rangle^2};$$

$$\epsilon_{AGN} = \frac{\sigma_{AGN}}{\sqrt{N_{spaxels}}} \tag{B.1}$$

where $N_{spaxels}$ is the number of spaxels considered to compute the averaged value within each galaxy group. We compute these quantities for the DP/MaNGA and the CS2 galaxies, divided in different sub-groups. The errors ϵ_{AGN} on the means are of order 10^{-5}: the mean values are well-defined quantities even though the scatter of the distribution is large. The statistical results are summarised in Tab. B.1. We observe an overall large scatter for each distribution and comparable values between the DP/MaNGA and the CS2 sample, but the means are systematically smaller for the non-central-AGN galaxies than for the central-AGN galaxies (in the GV and when considering all of them). Small numbers of red galaxies prevent any reliable comparison. Last, we do not detect any significant differences between the central and satellite galaxies.

Table B.1: Averaged AGN fractions weighted by the Hα fluxes and computed on all the spaxels with reliable signal (S/N > 3 for all the emission lines required for the f_{AGN} computation), with the rms value σ_{AGN} of each distribution. The galaxies defined as "most massive" are either isolated galaxies, or the most massive galaxies of the groups as defined in Sect. .

$\langle f_{AGN} \rangle$	DP/MaNGA (29)	CS2 (108)
Blue cloud galaxies	0.04 (0.08)	0.03 (0.09)
Green valley galaxies	0.18 (0.24)	0.17 (0.26)
no-central-AGN galaxies	0.12 (0.13)	0.04 (0.08)
central-AGN galaxies	0.22 (0.27)	0.38 (0.29)
Red sequence galaxies	0.64 (0.23)	0.19 (0.32)
Transition galaxies	0.18 (0.26)	0.12 (0.22)
No-central-AGN galaxies	0.05 (0.09)	0.01 (0.05)
Central-AGN galaxies	0.23 (0.28)	0.14 (0.24)
Most massive galaxies	0.12 (0.21)	0.03 (0.11)
Satellite galaxies	0.11 (0.17)	0.06 (0.15)

Appendix C: BPT diagrams for the CS2 sample

Figure C.1 displays the BPT for the CS2 galaxies organised in four categories as defined in Sect. 4.3 and in Fig. 19.
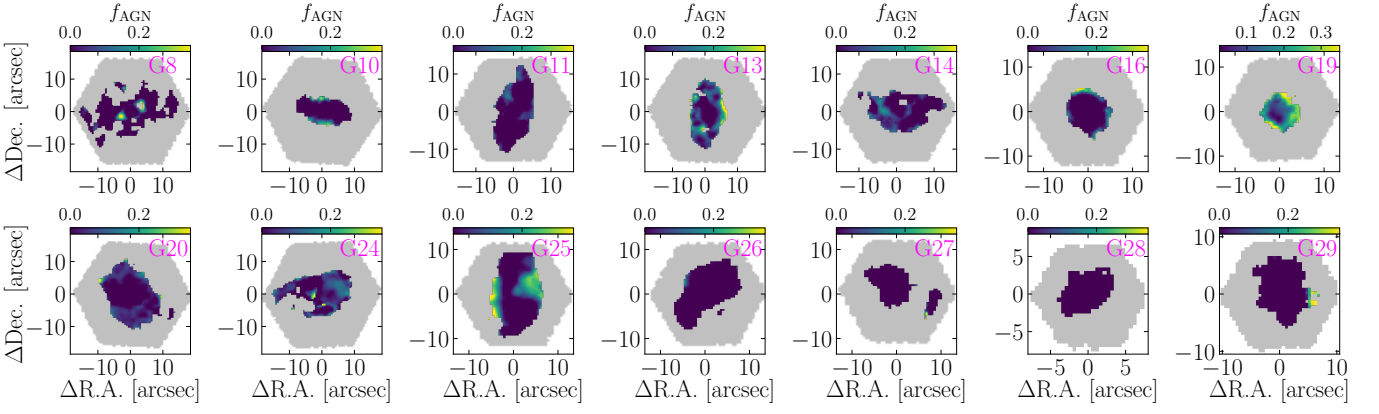
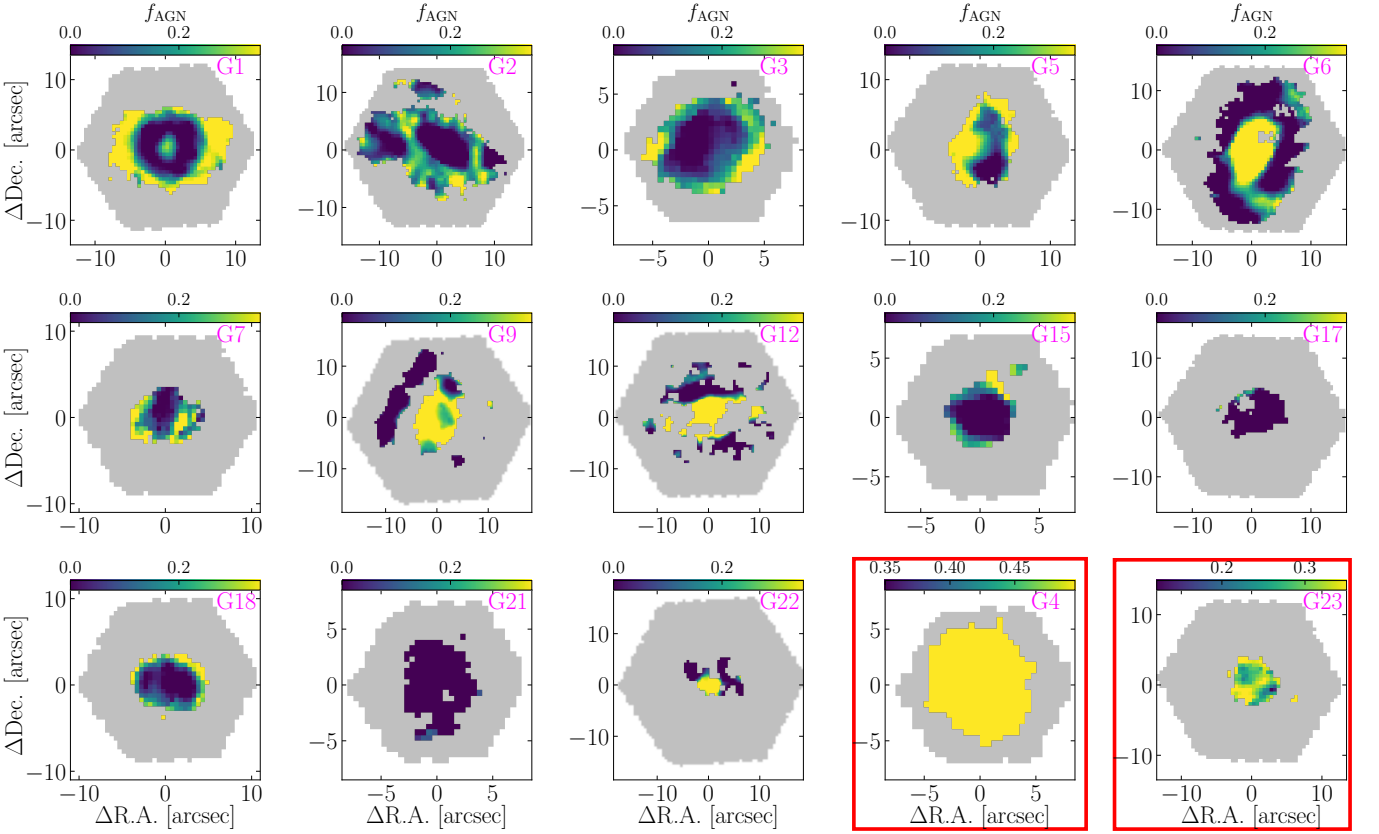Fig. B.1: f_{AGN} maps for the DP/MaNGA galaxies of the blue cloud.

Fig. B.2: Same as Fig. B.1 but for the green-valley and red galaxies. The red-sequence galaxies are displayed with red boxes. **The colourbar cannot be the same for G4 as its minimal AGN fraction is about 0.5.**
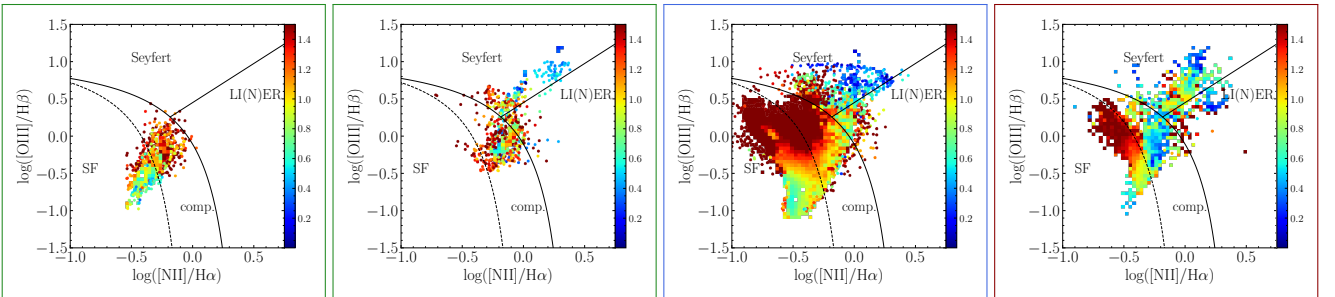

Fig. C.1: BPT diagrams for the galaxies of the CS2 sample. **Left:** GV galaxies without and with central AGN. **Right:** Blue-cloud and red-sequence galaxies. The colour indicates the distance to the centre, in units of R_e.